Dependence of the Interfacial Adhesion between Two Different Types of Material on their Electron Work Function and Electrical Conductivity

by

Raymond Christopher Setiawan

A thesis submitted in partial fulfillment of the requirements for the degree of

Master of Science

in

Chemical Engineering

Department of Chemical and Materials Engineering

University of Alberta

Abstract

Keywords: interfacial adhesion force, Electron Work Function, dipole layers.

We observed and investigated a novel interfacial phenomenon related to the dependence of interfacial bonding or adhesive force (F_{Ad}) between two substances on the difference in their Electron Work Functions (EWF) or $\Delta\varphi$ and developed a model to quantify such a dependence. First, using PEDOT:PSS/PEO nanofilm as a sample system with various wt./wt.% ratios of DMSO, we observed the dependence of its interfacial adhesion with Si_3N_4 (silicon nitride) on the nanofilm's conductivity and $\Delta\varphi$ of the system, determined through AFM analysis. It is shown that a larger $\Delta\varphi$ and higher conductivity of the polymeric nanofilm increase its adhesive force with silicon nitride. The second series of experiments using a similar method were performed for different pure metals with the objective to develop a theoretical approach in elucidating the quantitative correlation between F_{Ad} and $\Delta\varphi$ across the interface.

      This study demonstrates that the interfacial adhesive force is mainly governed by two factors: 1) the difference in EWF between the two materials in contact and 2) the electrical conductivity of the materials involved. The

former acts as the driving force for establishing a double dipole layer at the interface, leading to the electrostatic interaction, while the latter determines the easiness of the system to form the double dipole layers. This study demonstrates an approach to tailor interfacial bonding for different material types without atomic diffusion, promising for applications in various fields, e.g., better control of biomedical films on implants and functional films for electronic devices.

In the succeeding part, we established an analytical model to quantify the adhesive force (F_{Ad}) dependence between two different substances on their Electron Work Functions (EWF or φ) and conductivity without atomic diffusion involved. This model does not only help calculating the adhesive force but also elucidate the underlying mechanism.

Preface

No part of this work was taken from other people's or party's work without their prior consent, except otherwise noted as cited works used in this scope alone.

Some portions of this work have been published or presented in these scientific forums and journals/communications:

1. *Langmuir* (ACS – American Chemical Society Publications): Setiawan RC, Li DY. Tuning the Conductivity and Electron Work Function of a Spin-Coated PEDOT:PSS/PEO Nanofilm for Enhanced Interfacial Adhesion. *Langmuir*, 2021, **37**(16): 4924-4932.
2. Best Paper - Conference proceedings of the 5th International Conference of Theoretical and Applied Nanoscience and Nanotechnology (TANN'21) – Niagara Falls, Canada, 2021.
3. Conference proceedings of the 32nd Canadian Materials Science Conference (CSMC 2021) – Queen's University, Virtual Format.
4. The dependence of interfacial adhesion between substances on their Electron Work Functions, Raymond Christopher Setiawan, Mingyu Wu, D.Y. Li, *submitted*, 2021.

Dedication

To my father Sukamto (Yap Seng Tjai)
To my mother Melania M. Karnali (Lie Siok Lan)
To my friends Ung Tung Ho and Janieka Cendana

City of Edmonton, Province of Alberta, Canada,
in the Year Two Thousand and Twenty-One of Our Lord

Acknowledgments

This work was directed to address the fundamental relationship between the adhesive force, and Electron Work Function (EWF) influenced by the electrical conductivity for polymer/ceramic and ceramic/metal interfaces. This work would provide new insights into interfacial adhesion or bonding.

I would like to give my thanks and appreciation to the following persons:

Dr. Dongyang Li for his guidance and supervision. His insights on tribology and metal science are among the world's best. I had enjoyed being taught and supervised by him.

Dr. Xuehua Zhang, Dr. Chung Hyun-Joong, Dr. Hongbo Zeng, and Mingyu Wu, PhD, for their helpful insights on polymer and solid-state physics. Combining the two areas of material science is undoubtedly a challenging task, and should I be devoid of their help, I would not be able to form a rigorous discussion in this thesis.

Dr. Ta-Ya Chu (University of Toronto, Canada) for his mentorship through the CTSTA (Canada-Taiwan Science and Technology Association).

My cohorts Zhang Dong, Mohammadjavad Palimi, Xu Zhen, and Aakash Kumar, who always give me helpful thoughts on how to improve my experiments and avoid falling into technical traps.

Tung Ho Ung (Kuching, Malaysia), Janieka Cendana (Taipei, Taiwan), Iyit Benusia (Boston, USA), Elissa Chiuputri (Jakarta, Indonesia), Hannie Fransisca (Surabaya, Indonesia), and Elton Quek Ming Kai (Singapore) for giving me the reason to keep going forward. If ever I lost my interest, they were the ones that gave me new spirits.

Unfortunately, I cannot mention all my friends and families one by one here. However, do remember that you are always in my mind, and my thanks will always be yours.

This thesis does not mark the epitome of my pursuit of knowledge. I recognize that this is just a part of my long journey, but I have always cherished every part of it. For every fond memory I wrote and warm acquaintances I accrue, every tear I shed and every laughter I had, thank you, University of Alberta! *Quaecumque vera*: Whatsoever things are true!

<div align="right">

Author

Summer 2021

</div>

Contents

List of Tables

List of Figures

List of Abbreviations

1. ACN — Acetonitrile
2. AFM — Atomic Force Microscope(y)
3. AFS — Acoustic Force Spectroscope(y)
4. BioMEMS — Biological Micro-electromechanical systems
5. cAFM — Conductive Atomic Force Microscope(y)
6. CPD — Contact Potential Difference
7. DMSO — Dimethyl Sulfoxide
8. DOS — Density of States
9. EDL — Electrical Double Layer
10. EG — Ethylene Glycol
11. eV — Electron Volt
12. EWF — Electron Work Function
13. F-D — Fermi-Dirac (Statistics)
14. ITO — Indium Tin Oxide
15. KP — Kelvin Probe
16. KP-AFM — Kelvin Probe- Atomic Force Microscopy
17. L-J — Lennard-Jones (Law/Potential)
18. MEMS — Micro-electromechanical systems
19. MT — Magnetic Tweezer
20. MW — Molecular Weight
21. OP — Oliver & Pharr's (Indentation Method)
22. OT — Optical Tweezer
23. PANI-CSA — Camphorsulfonic Acid-doped Polyaniline
24. PDMS — Polydimethylsiloxane
25. PEDOT:PSS/PEO — Poly(3,4-ethylenedioxythiophene) Polystyrene Sulfonate/ Polyethylene Oxide

List of Symbols

1. A_c Contact area
2. A_I Integrated area
3. A_p Projected tip area at height h
4. A_r Atomic mass
5. D System's dimensionality
6. d Charge separation length
7. E Energy
8. e or e_o Elementary charge of an electron
9. E_C Energy level of conduction band
10. E_F Fermi energy
11. E_{Young} Young's Moduli
12. $f(E)$ Fermi-Dirac distribution
13. F_{Ad} Adhesive force
14. h Plank's constant
15. $\hbar$ Reduced Plank's constant
16. k_B Boltzmann constant
17. m_e Mass of an electron
18. m_o Mass of fermion
19. N Number of molecules
20. N_{Av} Avogadro's number
21. $N(E_F)$ The density of states at a given Fermi level
22. q_e Elementary charge of an electron
23. t Time
24. T Temperature
25. T_{Debye} Debye's temperature
26. T_o Characteristic temperature

xviii

Funding Disclosure:

Declaration of Competing Interest:

I acknowledge that this work in its entirety is free from any form of conflicting or competing interests.

COVID-19 Protocol:

Due to the disruptions caused by the global COVID-19 pandemic, some parts of this study were carried out remotely whenever possible. However, due to the nature of this study requiring some physical presence at the laboratory establishment, this work was conducted by strictly adhering to the university's COVID-19 propagation prevention protocol.

The author, as the principal executor of this study, strictly adhered to the instructions and bylaws issued by the Alberta and the Federal Governments related to the establishment closure and restriction to entry (March 2020, December 2020, and May 2021), who during those times carried out no laboratory works on and within the perimeter of the university establishments.

This thesis is registered under the *Theses Canada* program.

The University of Alberta acknowledges that we are located on Treaty 6 territory, and respects the histories, languages, and cultures of First Nations, Métis, Inuit, and all First Peoples of Canada, whose presence continues to enrich our vibrant community.

L'Université de l'Alberta reconnaît qu'elle est située sur les terres du Traité 6 et respecte les histoires, les langues et les cultures des Premières Nations, des Métis, des Inuits et de tous les peuples autochtones du Canada, dont la présence continue d'enrichir notre communauté si vivante.

Chapter I:
Introduction

This chapter outlines the issues that we are addressing and the motivation, significance, and underlying principles of this study. It also includes general approaches for all the problems presented and outlines the criteria for the study's success. The general outline for this study consists of two parts; the first part: practical exposition, explores the effect of increased conductivity and change in Electron Work Function in PEDOT:PSS/PEO polymeric nanosheet system toward its adhesion profile with Si_3N_4.

The second part: theoretical exposition, elucidates the effect of the Electron Work Function (EWF) of pure metals toward its adhesion behavior with Si_3N_4 quantitatively so as to provide a broad and all-encompassing theoretical background behind the correlation of the two properties in question.

1.1. Motivations

1.1.1. The prominence of interfacial adhesive force

The interfacial adhesive force between two materials co-joined together plays an essential role in maintaining the integrity and physical durability of the materials. For example, in composite materials, the interfacial adhesive force (hereinafter mentioned as F_{Ad}) binds two phases to support the composite system (i.e., PDMS/ceramic tubes) together [1, 13]. In other instances, materials such as PEDOT:PSS heterojunction-based solar cells [2] are highly dependent on interfacial adhesion to maintain the bonding

between the polymeric sheet and the base material. Questions such as whether the junction between PEDOT:PSS and the base material in the solar cell (i.e., crystalline silicon) is durable then arises, and by what mode -if any- such bonding takes place.

Another notable example is the area of tribology, such as the wear of materials. When two surfaces (without diffusion) are in dynamic contact involving vibrations, environmentally induced tear, friction, *et cetera*, the wear damage is affected by the interfacial adhesive force [3]. In this case, reduction of adhesion between the two surfaces in contact is preferred [4, 12]. Adhesive strength can exacerbate vibration and seizure of moving parts, thus leading to complete breakdown of the entire system [12].

Adhesive force is present when two particles interact and can be thought of as the force required to separate two different bodies already in contact [6-9]. Adhesive force is a form of attractive force [10-11]. Knowing the adhesive force between two surfaces is very critical in material design and selection. In other instances, adhesive force may be more vital in MEMS or BioMEMS applications since the size of the interface is very small (sometimes in the order of nanometers); hence the strength of adhesive force becomes more critical and prominent [14, 19]. Strong adhesion between surfaces may enhance the structural integrity of minuscule MEMS.

Currently, AFM apparatus can be used for adhesive force measurement in air and liquid by using a wide selection of cantilevers/tips (i.e., silicon nitride) [15-18]. By establishing contact between the AFM tip and the surface and evaluating the resulting piezo extension-retraction profile, one can infer F_{Ad}'s strength [21, 22].

Accurately measuring interfacial F_{Ad}, however, is not an easy task. To precisely measure F_{Ad}, one usually needs to immobilize a particle made of the material under study to a microscopic AFM cantilever and perform force curve analysis on the other surface (i.e., measuring the cohesive energy and quantifying the van der Walls (vDW) force between the two body [5]). This method is highly labor-intensive and rigorous, and not many AFM probes are readily available to be used to perform the experiments with such a

setting. However, understanding whether the adhesive force between two materials is strong or not is crucial for a researcher who wants to design a new heterojunction system consisting of interfaces between different materials with different properties, for instance.

There are several sources or mechanisms for adhesion: Mechanical (such as materials filling void/pores), chemical (covalent or hydrogen bond), physical (such as physisorption), electrostatic (different in electrical charge density across interface), and diffusive (adhesion inside bulk metallic alloy) [6, 10, 23]. In this study, the electrostatic adhesion mechanism (colloquially: *electroadhesion*) will be elaborated (see Chapter 2 - Chapter 4), and the theoretical background will be debated. This study was divided into two main experimental parts, 1) the probing of interfacial F_{Ad} between PEDOT:PSS/PEO and Si_3N_4 (see section 1.1.3 and Chapter III) to provide an empirical proof of the phenomenon and its practical usage; and 2) the probing of interfacial F_{Ad} between seven different pure metals with Si_3N_4 (see section 1.1.4 and Chapter IV) to provide a theoretical framework to quantify the correlation between interfacial F_{Ad} and materials' EWF under the influence of conductivity.

1.1.2. Gaps in current theories

Currently, no explicit theories can quantitatively explain the magnitude of electrostatic-driven adhesive force between two materials forming an interfacial bonding (attractive force that holds interface together). The leading idea developed around this subject is using a general mean-field theory that explains the influence of electrostatic attraction between two solids on the contact mechanics [24]. However, this approach did not address how the voltage drop across the interface occurs in the first place. Mechanistically speaking, some physical behaviors or properties that are innate to the material that influences the voltage drop across the interface, dictate how significant the voltage drop is, leading to *electroadhesion*

phenomena. Furthermore, there are generally limited findings explaining how bonding occurs in an interface where there is virtually no to limited atomic diffusion (i.e., a non-metallic system of interface). Some results have shown that differences in electrical charge density across an interface may create an interaction of materials manifested as bonding, however, the underlying mechanisms are not well clarified, and there are still gaps in the current theories or models. The elucidation of the mechanisms underlying such interactions is therefore deemed necessary.

Testing the adhesive force between two materials in a laboratory may be labor-intensive and sometimes defects the materials themselves [25]. Furthermore, there are no clear guidelines in place for an interfacial design that may assure the durability of the material or minimize the adhesive-related wear where the condition of the systems must prefer the minimization of adhesive force such as in drilling machine, etc. Presently, the guideline for material designs Hence, relating the adhesive force with a certain readily available physical revolves around material's macro-durability and properties, such as elasticity, Young's Moduli, etc. Finding new property directly related to the *electroadhesion* phenomena may also provide practical usage in a real-world application.

Our findings may provide new insights on the mechanisms of electrostatic-driven interfacial adhesion between two dissimilar materials of differing Electron Work Function (EWF). The magnitude of the force of adhesion can be correlated with three key physical parameters: the difference in EWF between the two materials, the conductivity, and the bulk charge density of the materials. The findings shown in Chapters III and IV may provide practical and theoretical insights into bonding due to electrostatic pressure. Furthermore, this correlation may help future researchers better control the interfacial bonding of novel materials and design a new interface.

1.1.3. Part I: Interfacial F_{Ad} between PEDOT:PSS/PEO and Si_3N_4 (practical exposition)

Polymers and ceramics generally have a low affinity for each other [26], which limits their applications when polymeric and ceramic conjugates are needed. The main objective of this part of the study is to investigate the effect of conductivity on the polymer's affinity for ceramic materials, which is expected or hypothesized to be governed by the interfacial work function and the establishment of a dipole layer at their interfaces.

Since PEDOT:PSS can gain elevated electric conductivity by DMSO addition [13], we chose PEDOT:PSS + DMSO as sample material for the current study. This study also helps extend the commercial applications range of PEDOT:PSS nanosheet films, such as in systems that involve polymeric-ceramic conjugates or interfaces. The underlying mechanism and effectiveness of adhesion between PEDOT:PSS with other types of material can hopefully be clarified and confirmed.

Here we report an observed novel phenomenon where one can increase the strength of intramolecular bonding for PEDOT:PSS by increasing its sheet's conductivity as a starting model. Moreover, we can attribute the effect of PEDOT:PSS sheet's conductivity on its bonding with Si_3N_4, as a sample pair system for study, through EWF analysis.

1.1.4. Part II: Interfacial F_{Ad} between pure metallic compounds and Si_3N_4 (theoretical exposition)

We demonstrate the adhesive force (F_{Ad}) dependence between two different substances on their Electron Work Functions (EWF or φ) without atomic diffusion involved. The adhesive forces between several metals and Si_3N_4 were measured using an Atomic Force Microscope (AFM). It is shown that the more significant the difference in φ between the two substances in

contact, the larger the F_{Ad}. An analytical model is proposed to elucidate the underlying mechanism and quantify the adhesive interaction.

Using pure metals for the study can avoid complications and thus provides a more theoretical insight into the interatomic interaction through the interface formed by the pure metal and Si_3N_4. We have further elaborated the metals we used in this study (Iron, Chromium, Manganese, Copper, Titanium, Vanadium, and Silicon), altogether with the resulting model obtained from this study included as part of the exposition.

1.2. Criteria for the Study's Success

1.2.1. Part I

This study seeks to provide insight into the effect of EWF and conductivity of PEDOT:PSS/PEO polymeric nanosheet on its adhesive force attracting Silicon Nitride to offer a practical usage on the said correlation in real life.

1.2.2. Part II

This study seeks to provide a theoretical model to quantify the effect of EWF, conductivity, and bulk charge density of different pure metals on their adhesion with Silicon Nitride surface to provide a feasible and sound model that can be used to generalize the behavior of interfacial adhesion.

1.3. Timeline

Table 1.1. *Timeline table of this study.*

Project description	Timeline
Proposal, preparation	Sept. 2019 – Oct. 2019
Part I: PEDOT:PSS/PEO	Nov. 2019 – Aug. 2020
Part II: Pure metallic compounds	Jan. 2021 – Jun. 2021
Project closing	Jul. 2021

1.4. Outline of this thesis

This thesis consists of 5 (five) chapters: Chapter I 'Introduction', Chapter II 'Theoretical Background', Chapter III 'PEDOT:PSS/PEO adhesion profile with Silicon Nitride', Chapter IV 'Pure metal adhesion profile with Silicon Nitride', Chapter V 'General Conclusions,' which includes the conclusions, future works, recommendations, and remarks.

The graphical abstracts for this study are also provided in the appendix of the thesis.

Chapter II:
Theoretical Background

This chapter presents some previous studies related to the investigation being conducted that form a part of this thesis. Some preceding works and theories will also be debated. First, the adhesion and Electron Work Function probing theory will be presented, including adhesive force measurements using Atomic Force Microscopy (AFM) with the Kelvin Probing (KP-AFM).

Furthermore, the effect of adhesive force on the tribological behavior of materials will be reviewed. The application of PEDOT:PSS functional polymer, which is used in the present study, in several areas will be introduced, including how the adhesive force might be able to be ameliorated so as to provide a system with better mechanical integrity.

2.1. Adhesion
2.1.1. Definitions

Adhesive force is the attractive force that binds two dissimilar materials together, which equals the force to separate them if such materials possess the tendency to cling to one another [27]. IUPAC defines adhesion as the attachment of a substance to the surface of another substance [28]. Such adhesion may take place given sufficient energy (chemical or physical) is applied as linkages. Physical linkage is reversible given enough energy is applied to reverse the said adhesion process [28].

2.1.2. Surface energy and adhesion as work of cleavage

For two materials to maintain/sustain a cojoined state, a finite amount of energy is needed. This energy is known as surface energy, loosely defined as the work required to form an area of a surface. When two surfaces converge to develop an interface, their surface energy will affect the work required to cleave the cojoined interface, conventionally called cleavage energy/work [10, 29].

Given two identical surfaces of the same material with a surface energy γ (J or kg m²/s²), the work of cleavage W^{cl} in a vacuum is defined as:

$$W^{cl} = 2\gamma \tag{2-1}$$

The above definition only considers a particular condition where two surfaces are identical in properties, morphology, and materials.

For a general approach where two surfaces forming an interface is made from dissimilar materials 1 and 2, one may apply the Young-Dupré correlation [30]:

$$W_{12}^{cl} = \gamma_1 + \gamma_2 - \gamma_{12} \tag{2-2}$$

where W_{12}^{cl} is the cleavage work required to cleave cojoined surface 1 and 2 (Fig. 2.1), γ_1 and γ_2 is the surface energy of material 1 and 2, respectively, and γ_{12} is the energy of the formed interface between material 1 and 2. Note that when material 1 = material 2:

$$\gamma_{12} \; when \; 1 = 2 \; \rightarrow \; \gamma_{12} = \gamma_{11} = 0 \tag{2-3}$$
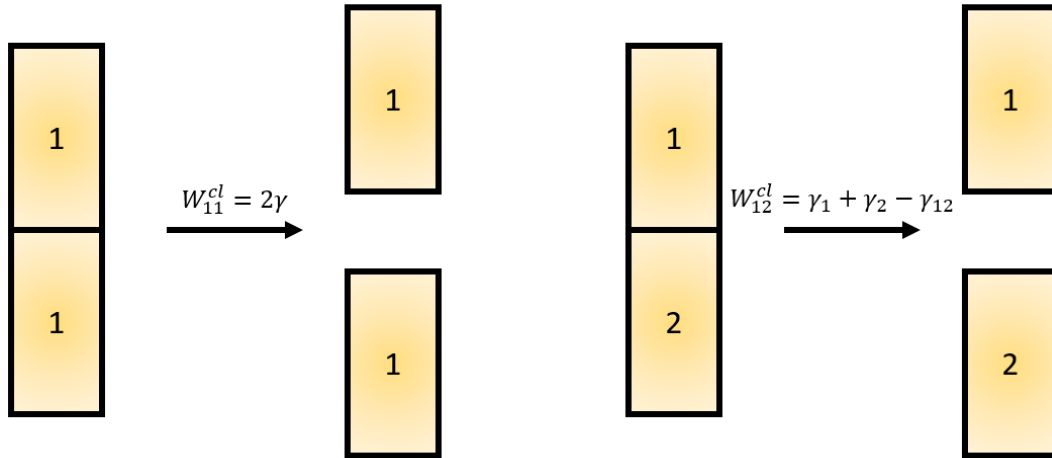
Figure 2.1. *Representation diagram for two cases of cleavage in vacuum (between two identical surfaces and two dissimilar surfaces).*

When an interface is to be cleaved apart in a medium of an index value of 3 (in a non-vacuum media), the cleavage energy can be evaluated by using the work equilibrium approach as indicated below:

Looking at Fig. 2.2, on the left-hand side, we have a cojoined 1-2 system inside an arbitrary gas as an example (denoted as 3), where then it is separated by a work W_{132}^{cl}:

$$W_{132}^{cl} = \gamma_{13} + \gamma_{23} - \gamma_{12} \qquad (2-4)$$

The equation (2-4) is different from the thermodynamic energy (or work) required to remove interface 1-2 in a vacuum medium as expressed by equation (2-2).
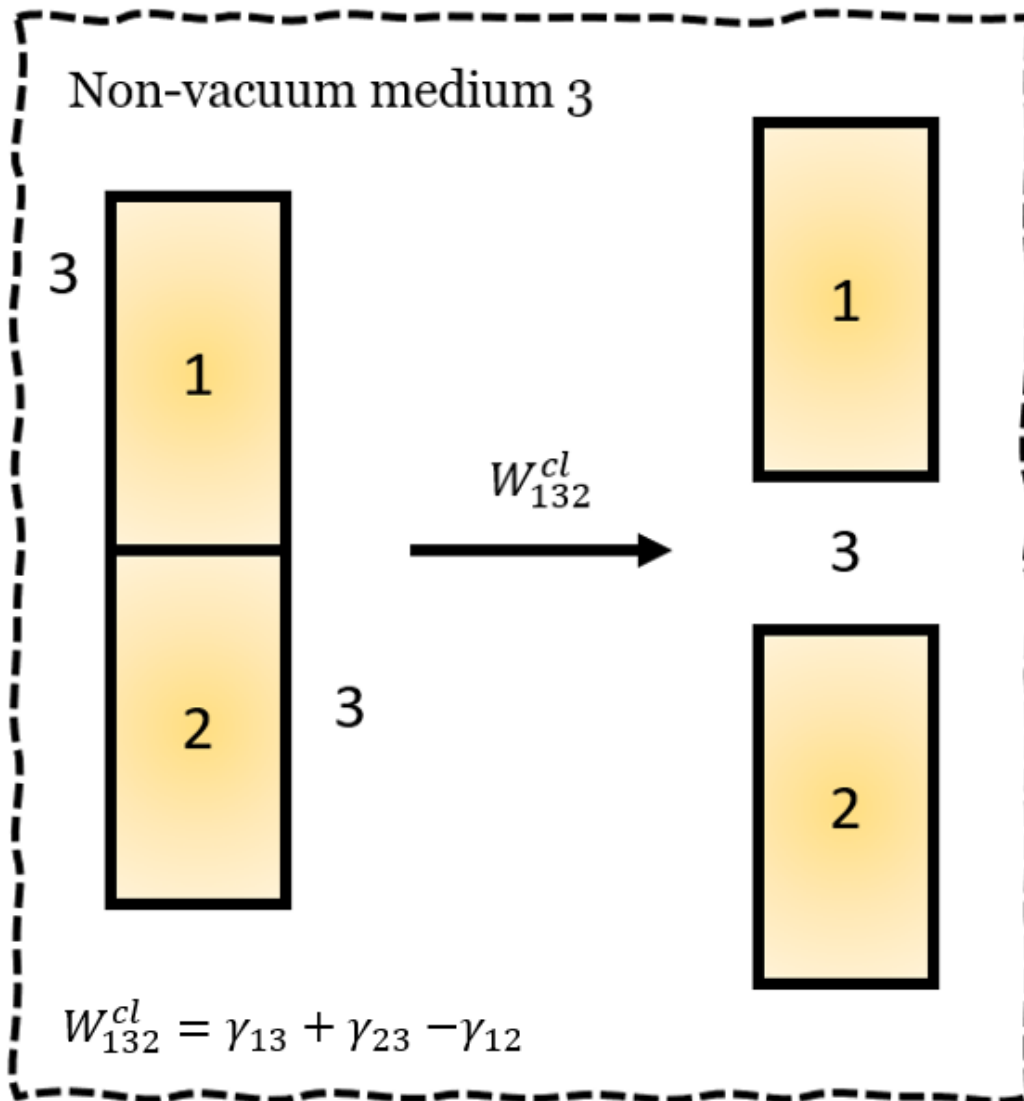
Figure 2.2. *The work required to separate interface of dissimilar cojoined materials inside a non-vacuum medium.*

2.1.3. Mechanisms

Adhesion is an umbrella term that encompasses different types and mechanisms of adhesive interactions. There are several different mechanisms, namely chemical [31], mechanical [32], dispersive [33], electrostatic [1], and diffusive [34]. Although electrostatic adhesion is the main subject of this study, the basic principles of each mode of adhesion will be debated and elaborated concisely here.

Table 2.1. *Different mechanisms of adhesion based on their underlying principles.*

Mechanism	Underlying principles
Chemical	Chemical bonding between two interfaces, such as covalent or ionic bonding, hydrogen bonding with materials containing hydrogen (H), oxygen (O) and fluorine (F).
Mechanical	By interlocking. Materials with microscopic hills and valleys, pores, or voids may interlock together and thus forming a cojoined interface, a.k.a. tethering.
Dispersive	By physisorption through vdW (*van der Waals*) interactions, two materials are slightly polarized and form a hotspot in a certain region, inducing it to be slightly positively charged and the other negatively charged. Another example includes the *London Dispersion*.
Electrostatic	Forming electrical charge/electrical double layer across the interface, such as the capacitor effect.
Diffusive	Two materials are cojoined together by merging through diffusion, e.g., metallic alloy. This can be thought of as mechanical tethering at the molecular level.

2.1.4. Methods for force spectroscopy

Several methods have been established to measure the adhesive force between two materials. Such practices have been referred to by using 'force spectroscopy' as the umbrella term. Several techniques that have already been employed to probe the force spectroscopy includes -but not restricted to- Atomic Force Microscopy (AFM) [11], Magnetic Tweezers (MT) [35], Optical Tweezers (OT) [36], bio-membranes [37], Acoustic Force Spectroscopy (AFS) [38], and microneedles (μ-needles) [39].

The underlying differences in practical application and principles of the aforementioned will be elaborated on here.

Table 2.2. *Methods for measuring adhesive force based on their underlying principles.*

Techniques	Underlying principles
AFM	Utilizes a small probe mounted on a cantilever. The laser detects the deflection of the cantilever from the overhead of the apparatus. Upon contact with the surface of interest, it may deflect in response to the intermolecular attractive and repulsive forces found in the proximity to the sample.
MT	Manipulation of paramagnetic beads using a gradient of the magnetic field. The particle of interest can be deflected into a surface and then retracted, after which the force/resistance can be detected.
OT	Using a highly focused laser beam to manipulate and move small objects in 3D and direct them to a surface of interest, where the adhesive force can be detected as a resistance from the particle to move away from the surface.

Bio-membranes	Usually used to measure cell adhesion in biological settings. A surface with specific topography is used as cell attachment media and used to measure the adhesive force of the cell by measuring the shape, concavity, and curvature of the membranes.
AFS	Applying a small number of forces (usually piconewtons) to specific particles until the particles are moved from the surface. From the reading, one may be able to infer the adhesive force.
μ-needles	Microneedles are directed to a particle adhering on the surface and push away the said particles until the particles are removed from the vicinity of the surface. A piezo component is used to measure the deflection of the microneedles and used to infer the adhesive force.

2.1.5. Atomic Force Microscopy (AFM)

AFM works using a tip mounted on a cantilever (Fig. 2.3), bringing it close to the surface, which may or may not contact the surface depending on its mode. A laser beam is projected onto the cantilever coated with a highly reflective material (such as PtIr – Platinum Iridium coating), and the laser beam is reflected onto the photodetector. A change in the cantilever deflection may be translated into the deflection of the light signal reflected and may be interpreted as the z or height signal of the AFM tip [11, 40].

In contact mode, the AFM tip will be slightly pushed down the surface, creating a deflection signal detected through the piezo material. The light reflected may tell the apparatus whether the cantilever has touched the material and when to stop exerting forces. A fixed amount of cut-off force is set, and the cantilever is pushed up until the maximum allowed value has been achieved.

After that, the AFM cantilever is retracted, where some resistance is observed due to the work of adhesion. The trace and retrace signal are thus obtained from the piezo material, and the adhesive force can be inferred from the reading.
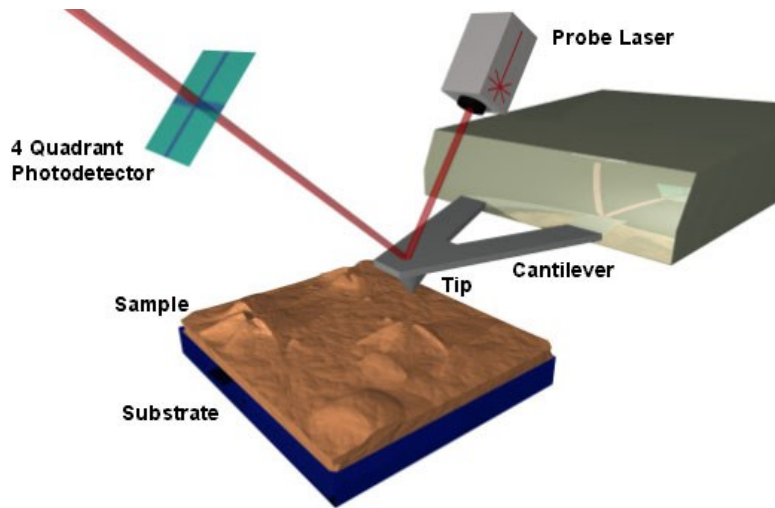
Figure 2.3. *Schematic diagram and representation of Atomic Force Microscopy setup [41].*
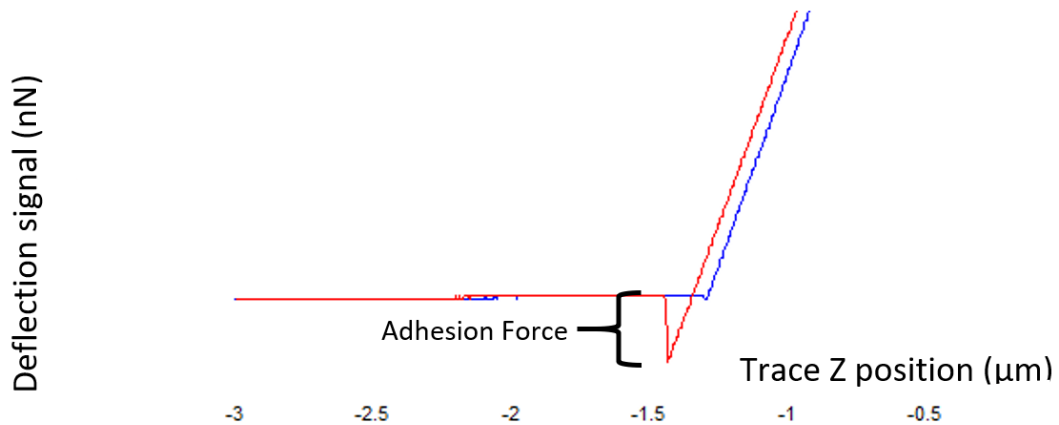
Figure 2.4. *Trace and retrace curve of the contact mode AFM (deflection to displacement)*

A small gap from the piezo reading shown in Fig. 2.4 represents the inertness of the cantilever tip when it is retracted back due to the influence

15

of the work of adhesion imposed by the surface to the cantilever tip. The deeper the groove, the higher the deflection degree and the stronger is the adhesive force.
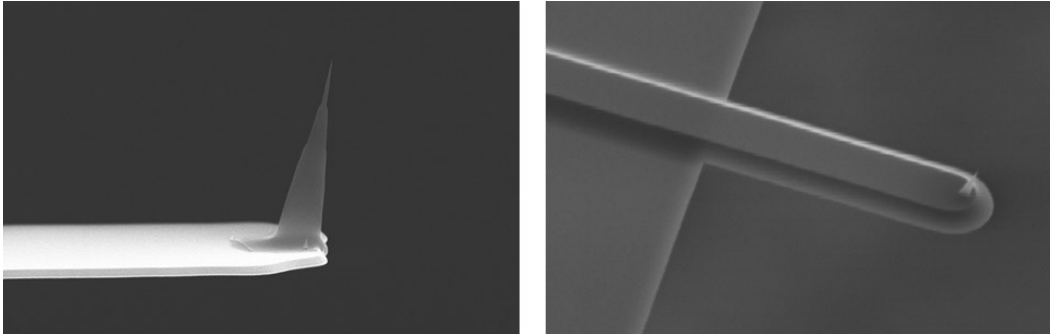
Figure 2.5. *SEM of an amorphous silicon-rich silicon nitride (Si₃N₄) cantilever with a thickness of 99 nm, 13 μm length, and 4 μm width [42].*

AFM cantilevers can be tailored to meet practical needs, such as tips modified with certain biomolecules to measure the molecules' adhesion with cells (such as biotin) or different polymers and materials of interest. However, the most common and industry-standard application is the silicon nitride tip.
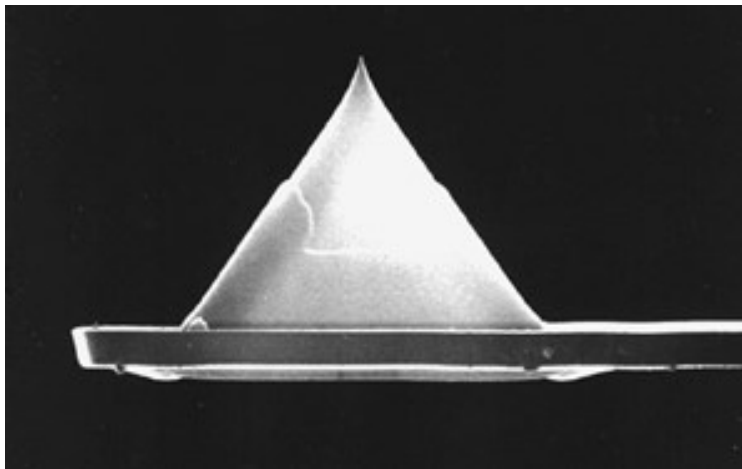
Figure 2.6. *SEM of a sharpened pyramidal silicon nitride (Si₃N₄) tip with a width of 400 nm and height of 2.9 μm, tip's Ø less than 20 nm, angle ~ 25-40 deg. [43]*

Two commonly used traction-separation relations can be used to analyze the adhesion from the AFM measurements: the Dugdale Traction-Separation Law; and the Lennard-Jones Traction-Separation Law [44].

The Dugdale Traction-Separation Law assumes that the adhesive stress η_D is constant over a fixed separation range, h_{Ad}, which then suddenly drops to zero after a certain height or retraction distance. The work of adhesion W_{Ad} is defined as:

$$\eta_D = \frac{W_{Ad}}{h_{Ad}} \qquad\qquad (2-5)$$

On the other hand, the Lennard-Jones Traction-Separation Law considers the relative change of the stress for different separation distance s, that is to say, that the stress η_{L-J} is a function of s. The said traction-separation relation can be described as:

$$\eta_{L-J}(s) = \frac{8W_{Ad}}{3z_0}\left[\left(\frac{z_0}{s+z_0}\right)^3 - \left(\frac{z_0}{s+z_0}\right)^9\right] \qquad\qquad (2-6)$$

where z_0 describes the range of the adhesion.
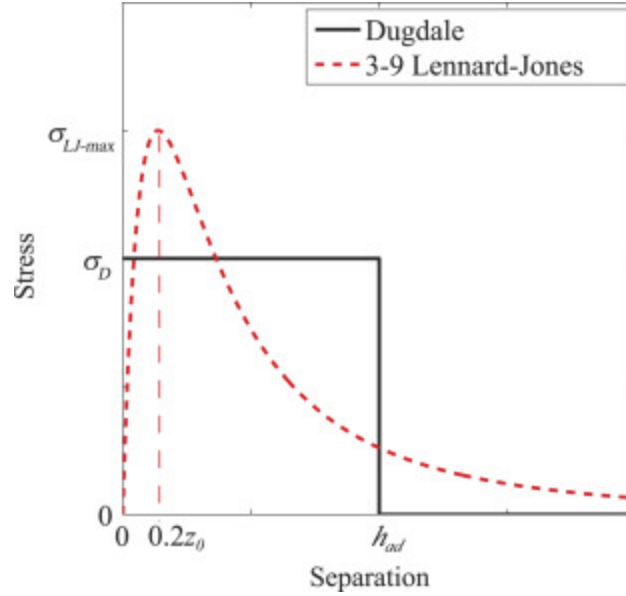
Figure 2.7. *The schematic representation of Dugdale and L-J Laws (both areas under the curve is identical).*

To calculate the force, one can simply integrate the adhesion stress with respect to the projected tip area at the height h (A_p (h)):

$$F_{Ad} = \int_{dA} \eta dA_p\,(h) \qquad\qquad (2-7)$$

where h is the measure of distance from the apex of the tip to the surface.

Hence, for Dugdale Traction-Separation Law, the adhesion force can be evaluated as:

$$F_{Ad} = \int_{dA} \eta_D dA_p\,(h) = \eta_D A_p(h_{Ad}) \qquad\qquad (2-8)$$

As for the Lennard-Jones Traction-Separation Law, the adhesion force can be evaluated as:

$$F_{Ad} = \int_{dA} \eta_{L-J} dA_p \, (h)$$

$$= \frac{8W_{Ad}}{3z_0} \int_{dA} \left[\left(\frac{z_0}{s+z_0} \right)^3 - \left(\frac{z_0}{s+z_0} \right)^9 \right] dA_p = \frac{8W_{Ad}}{3z_0} A_I \quad (2-9)$$

where AI represents the remaining integral term and is obtained by numerical method estimation, integrating from the lower boundary of h = 0 to a certain cut-off separation value of h = $5z_0$.

The calculated work of adhesion and its adhesion force value will not be altered significantly if an immense cut-off value is considered or assumed in the calculation. The physical interpretation for choosing such a cut-off value is that the stress will be ~1% of the peak stress value.

2.2. Electron Work Function (EWF)

2.2.1. Definition

Electron Work Function (EWF or φ) is defined as the minimum energy required to move an electron at the Fermi level inside material to its surface devoid of any kinetic energy [45].

Suppose the said electron is exited to a certain distance adjacent to the material's surface, whereby the said electron is no longer affected by the nuclear attraction force coming from the bulk interior of the material. In that case, the corresponding distance is defined as the critical distance. The energy required to remove the electron from the inner cavity of the atom to this critical distance can also be interpreted as the EWF.

$$\varphi = -e\phi_{vacuum} - E_{Fermi} \qquad\qquad (2-10)$$

where e is the elementary charge, and Φ is the electrostatic potential in the vacuum immediately outside the solid's surface, E_{Fermi} is the Energy at the Fermi Level [45, 46].

When two bodies are in thermal equilibrium and in a vacuum, albeit their Fermi level is the same, their work functions differ. As such, an electrostatic potential will be established across the boundary of the bodies, where it acts as the driving potential (-e x Φ_{vacuum}) for the electron transfer from one body having lower EWF to the other body having the higher EWF. Φ_{vacuum} is expressed as:

$$\phi_{vacuum} = V - \frac{\varphi}{e} \qquad (2-11)$$

where V is the measured voltage of the material relative to a ground with an established Fermi level equals zero.
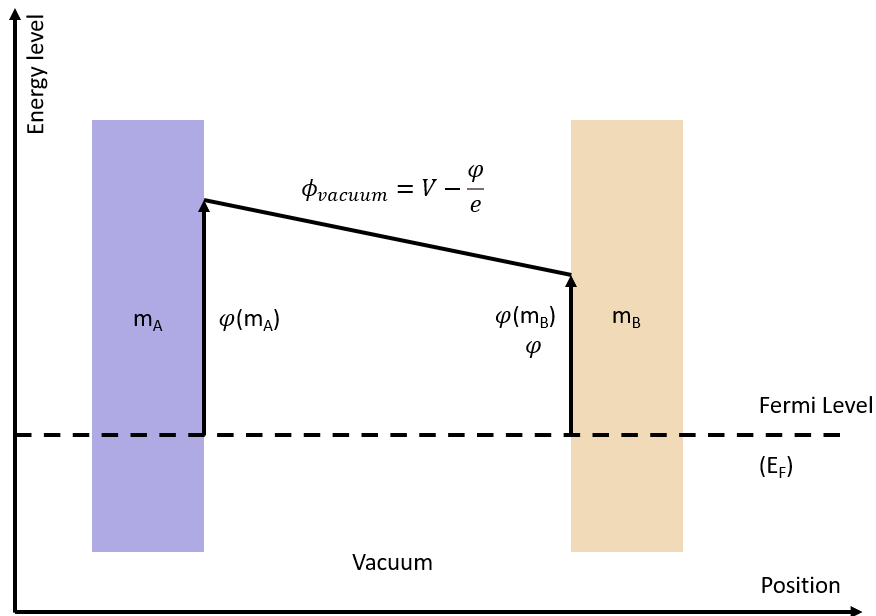
Figure 2.8. *Diagram representing the electrical potential drive across vacuum for two bodies having different work functions.*

2.2.2. Fermi energy

Fermi Energy (E_F) can be defined as the energy difference between the highest and the lowest occupied states of an imaginary quantum system consisting of a single-particle-in-a-box system devoid of mutually interacting fermions. Such a system is defined at 0 K (absolute zero temperature).

In a non-relativistic system of a non-interacting ensemble of identical spin-½ fermions, the Fermi energy is given as [45-47]:

$$E_F = \frac{\hbar^2}{2m_0} \left(\frac{3\pi^2 N}{V} \right)^{\frac{2}{3}} \qquad (2-12)$$

where $\hbar$ is the reduced Plank's constant ($\hbar$ = h/2π; hence $\hbar$ = 6.582119569...x 10^{-16} eV·s), m_0 is the rest mass of each fermion, N is the number of particles, and V is the volume of the system.

The Fermi-Dirac (F-D) Statistics gives rise to the Fermi function f(E), the probability that a particular energy state will be occupied by an electron at a given temperature, and is provided as:

$$f(E) = \frac{1}{e^{\frac{E-E_F}{k_B T}} + 1} \qquad (2-13)$$

where e represents the Euler's number (2.71828...), E represents a certain energy, E_F the Fermi energy, k_B is the Boltzmann's constant (1.38064852 x 10^{-32} m^2·kg·s^{-2}·K^{-1}), and T is the absolute temperature of the energy state (K). It is worth noting that the Fermi function is sigmoidal.

2.2.3. EWF and Young's Modulus

Previous works show that Electron Work Function (EWF) can be used as a probe to determine material's properties [48, 49], of particular interest is a crystalline material with properties that depend heavily on temperature, such as Young's Modulus. The correlation between EWF and temperature is given by the following model:

$$\varphi(T) = \varphi_0 - \alpha \frac{(k_B T)^2}{\varphi_0} \qquad (2-14)$$

where $\varphi(T)$ refers to the EWF at a certain temperature T (K), and φ_0 is the EWF at absolute zero temperature, i.e., $\varphi_0 = \varphi(T = 0K)$.

It has been shown that the Young's Modulus has a sixth power relation with the EWF, e.g. $E_{Young} \propto \varphi^6$.

α depends on the crystalline structure and based on this model α-T relationship can be established and used to further investigate the behavior of temperature toward the Young's Modulus.
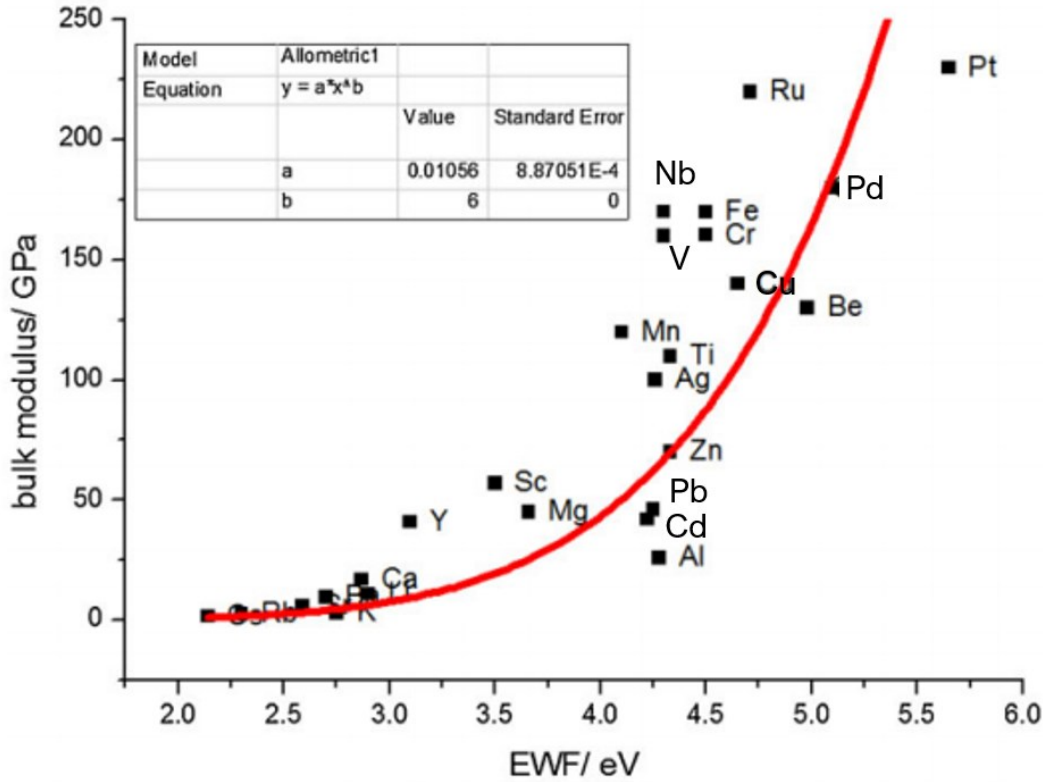
Figure 2.9. *Correlation between a material's EWF and its bulk moduli [49].*

2.2.4. EWF and thermionic emission

Another good use of work function is to determine thermionic emission (liberation of electrons from an electron-emitting body which is solely caused by the temperature of the electron, such that the energy required for the emission is primarily supplied from the heat energy) [49].

The current density for the thermionic emission (J_{th}) can be formulated as (by referring to the φ_{gap}):

$$J_{th} = AT^2 e^{-\frac{\varphi_{gap}}{k_B T}} \left(e^{\frac{q_e V}{k_B T}} - 1 \right) \qquad (2-15)$$

and A:

$$A = \frac{4\pi m_e k_B^2 q_e}{\hbar^3} = 1.20173 \; x \; 10^6 A \; m^{-2} K^{-2} \tag{2 - 16}$$

where m_e and q_e refer to the mass and charge of electron, respectively, and V refers to the potential applied.

2.2.5. EWF and thermal properties of a material

Previous works also showed a strong correlation between a material's EWF with its thermal expansion, given by the correlation using Lennard-Jones potential. The reciprocal of thermal expansion coefficient obeys a sixth power relationship with EWF [49].

Furthermore, EWF can also be correlated to the material's heat capacity by using Debye's model:

$$C_V = 9Nk_B \left(\frac{T}{T_{Debye}}\right) \int_0^{\frac{T}{T_{Debye}}} \frac{\xi^4 e^\xi}{(e^\xi - 1)^2} \, d\xi \tag{2 - 17}$$

and where C_V is the heat capacity at constant volume, T_{Debye} is the Debye temperature defined as:

$$T_{Debye} = \frac{\hbar \omega_{Debye}}{k_B} \tag{2 - 18}$$

where ω_{Debye} is the Debye frequency, proportional to the velocity of elastic wave in a solid; and where ξ is a parameter defined as:

$$\xi = \frac{\hbar \omega}{k_B} \tag{2 - 19}$$

It has been shown that $T_{Debye} \propto \varphi^3$.
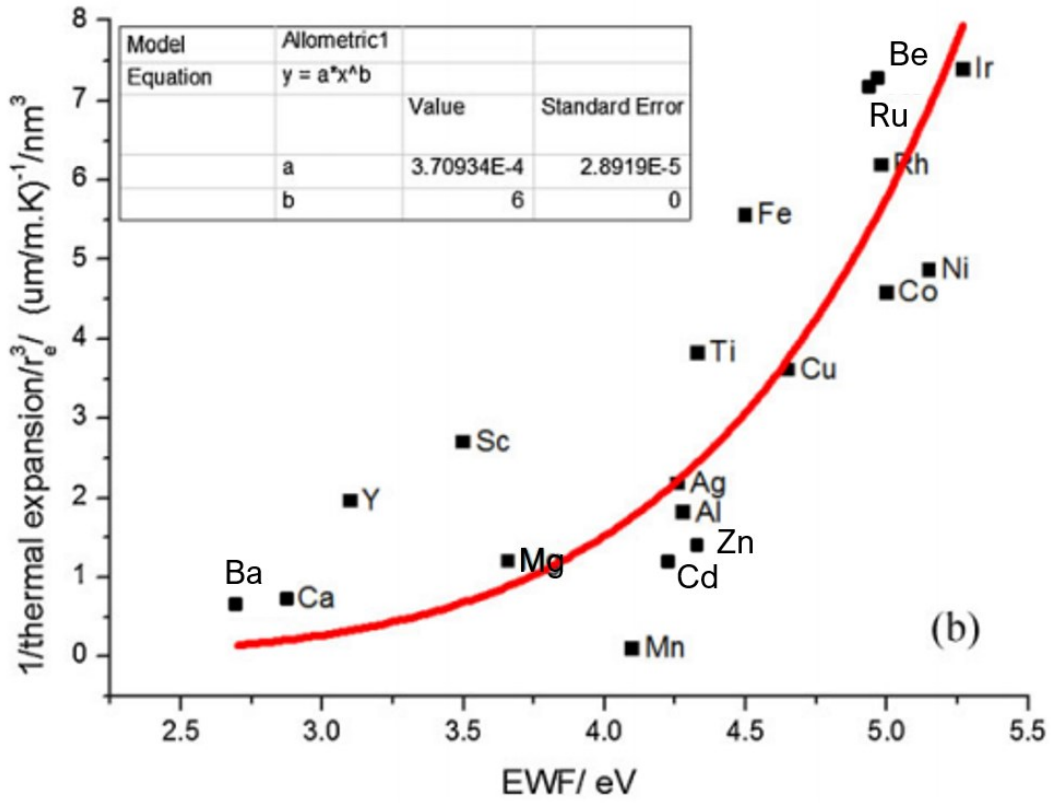
Figure 2.10. *Correlation between a material's EWF and its thermal expansion coefficient [49].*
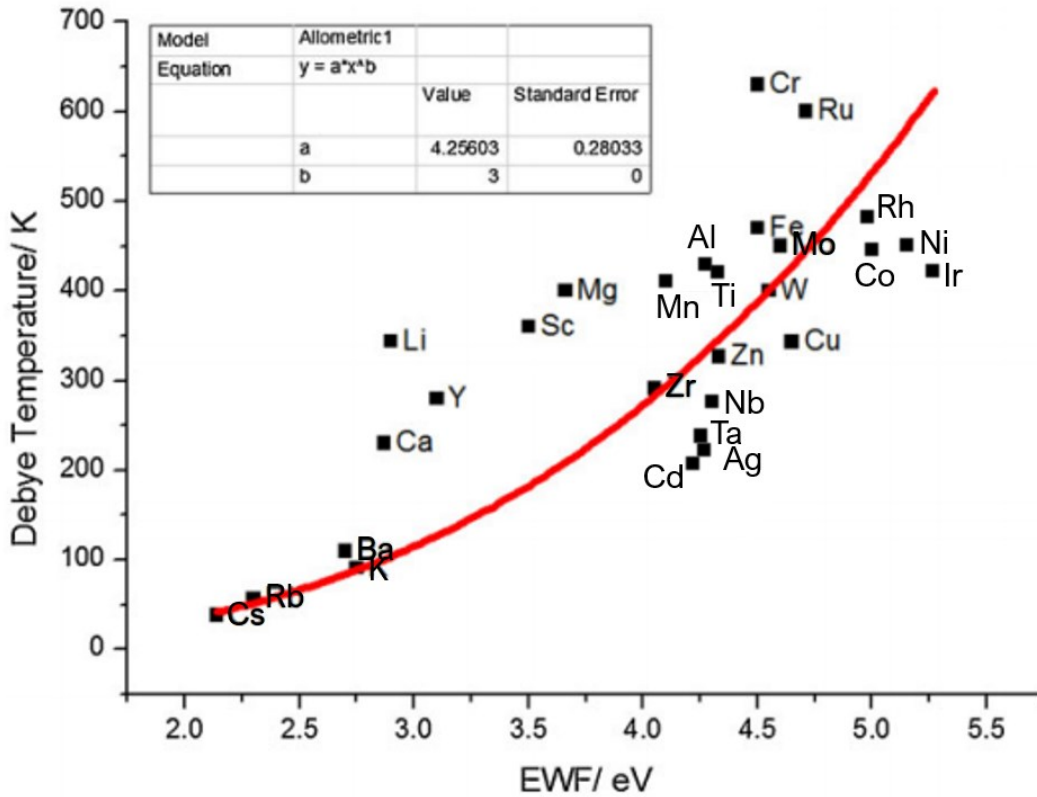
Figure 2.11. *Correlation between a material's EWF and its Debye Temperature [49].*

2.2.6. EWF measurement using Kelvin Probe Method

Kelvin Probe (KP) is a method used to measure the work function of a material's surface. It can be done in several ways, but the most prominent one being [117]:

A. Using tapping-mode AFM that is modified to cater for KP measurement. A conducting cantilever is used to scan the surface of interest at a constant height (hence non-contact mode) to obtain both the topography map and the work function map of the materials. Therefore, the obtained work function will be the local work function [51].

B. Using a specialized Kelvin Prober. The obtained work function will be a global value (meaning it does not measure each individual point's value or map the work function distribution) [52].

For both applications, the techniques and principles are the same. The probe is positioned very close to the surface and is perpendicular to the surface. The probe vibrates along the z-axis, with the average distance traveled denoted as Δz. Since the probe is conductive, it forms a parallel plate capacitor. The probe must be made from a different material from the sample's surface since the Fermi level of the two materials must be distinctive from each other [53-54].
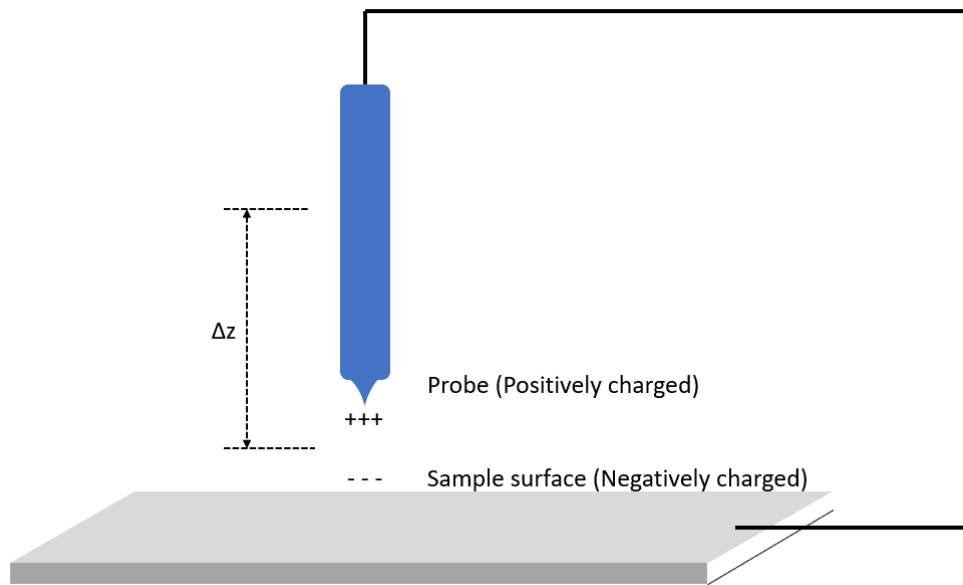
Figure 2.12. *The diagram representing the principle of Kelvin Probe Microscopy.*

As mentioned earlier, an electrostatic potential gradient will occur across the interface, and charge transfer occurs in the direction of the lower Fermi level to the higher Fermi level. After some time, an equilibrium of charge will be achieved, where then a surface charge will be detected and referred to as contact potential V_c. The vibration may cause the change in

the surface charge, creating an AC profile in the form of a sine wave, where it is demodulated to a DC signal. Once the DC potential is known, a backing potential (V_b) is applied to nullify V_c (that is to say V_b = - V_c).

The difference between the work function of the two surfaces is represented as the *Contact Potential Difference* (V_{CPD}) and is correlated to the DC and AC potential and applied potential V as:

$$V = (V_{DC} - V_{CPD}) + V_{AC} \sin(\omega t) \qquad (2-20)$$

where ω is the frequency of the resonance.

Since V_{DC} is applied to nullify the V_{AC} and therefore the frequency of the resonance, therefore the value of V_{DC} that minimizes ω corresponds to V = V_{CPD}, thus:

$$-eV_{CPD} = \varphi_{surface} - \varphi_{cantilever} \qquad (2-21)$$

where e is the elementary charge [55].

Chapter III:
PEDOT:PSS/PEO Polymeric Nanosheet Interfacial Adhesion with Si$_3$N$_4$ Surface

PEDOT:PSS (poly(3,4-ethylenedioxythiophene) polystyrene sulfonate (see Fig. 3.2**A**) is a polymer with an endless π-bond system in its backbone [56], rendering it intrinsically electrically conductive and thus can be used as an excellent medium to transfer electrons [57]. It has high thermal stability [58], high water dispersibility [59], and high transparency [60]. The electrical conductivity of PEDOT:PSS is well understood [61], and the material has found a wide range of applications such as touchscreen [64], electrical paper [63], etc. [65-69]

Due to its good biocompatibility, PEDOT:PSS has also been used as a scaffold for cell growth and tissue engineering [62], ranging from biomedical stent's coating to complex nanofiber network produced by electrospinning as a conductive scaffold for nerve cells differentiations. Studies have shown that PEDOT:PSS may be used as a base material to be electro-spun and be made to be nanofibrous with uniforms orientation [66].

Lately, PEDOT:PSS has been used as a coating for biomedical implants to increase cell's adherence to the surface and decrease the non-fouling properties of certain metals [67]. Due to its electroconductivity, PEDOT:PSS can be used as the interface between the medical implants and nerve cells growth since nerve cells respond well to electrical stimulation [68]. By conducting biphasic sinusoidal waves through the interface, the

growth of nerve cells can be enhanced, and its nerve-cell specific gene expression ameliorated.

In other fields, PEDOT:PSS has also been used as a coating for solar cells due to its transparency and high conductivity [69]. Currently, PEDOT:PSS/Si hybrid solar cell has achieved a Power Conversion Efficiency (PCE) of over 13% [70]. It is given that a higher PCE is very desirable in this context for solar cell applications. Should PEDOT:PSS be made semiconducting (p-type), a Schottky Diode will form upon contact with the base metal due to the difference in EWF (Electron Work Function) present across the interface. A dipole layer may form at interfaces to enhance interfacial bonding without diffusion involved [71].

With a post-treatment using methanol as an agent, PEDOT:PSS's conductivity can be increased from 0.3 S·cm^{-1} to about 1,362 S·cm^{-1} [72]. Other solvents can also be used with differing effects on PEDOT:PSS conductivity. For instance, an H_2SO_4 post-treatment can make the conductivity as high as 4,380 S cm^{-1} [73]. The addition of highly polar organic solvent with high boiling temperatures such as DMSO (Dimethyl Sulfoxide), EG (Ethylene Glycol), and Zonyl surfactant FS-300 can also extremely ameliorate the conductivity of PEDOT:PSS [74]. With the treatment using cosolvents (mixture of polar solvents with water, such as THF (Tetrahydrofuran) and ACN (Acetonitrile)), the sheet conductivity of PEDOT:PSS can be further increased. Yijie Xia and Ouyang J. [75] explained the observed phenomena with the Variable-Range Hopping Model (VRHM) that correlates the increased conductivity with the rearrangement of intramolecular orientation within the polymer nanosheet, hence reorganizing the Density of States (DOS) and the Fermi Energy (E_F) altogether.

In this study, we chose PEO (Polyethylene Oxide) as a natural polymer to be blended with PEDOT:PSS aliquot to increase the aliquot's viscosity and ability to be spin-coated so that it can be made a nanofilm. Naturally, the elongation at break of the resulting polymer will be increased (to about 280%) [72, 105], as with the introduction of other similar

polymers such as PMMA (Polymethylmethacrylate) [78] or PVA (Polyvinyl alcohol) [72, 77].

A uniform nanosheet with a highly similar intramolecular adhesion force may be produced by strictly controlling the nanosheet thickness and PEDOT:PSS to PEO ratio [79]. Therefore, the observed difference in adhesion is contained to one degree of variable change of the ratio of PEDOT:PSS/PEO to DMSO. A more elaborate model could be developed to understand the effect of conductivity on intramolecular adhesion and the interfacial bonding for conductive polymeric materials.

The application of PEDOT:PSS has been negatively affected because PEDOT:PSS does not form a robust bonding with other surfaces or substrates [76], rendering it severely deteriorated after prolonged exposure to the open environment or physiological fluids. The mechanism underlying the intramolecular adhesion strength and adhesion between the interface of PEDOT:PSS with non-conductive entities needs to be elucidated to tailor the adhesive bonding.

The objectives of this study are 1) to identify the key parameters that govern the interfacial adhesion between the PEDOT:PSS and silicon nitride as a sample system, 2) to elucidate the underlying mechanism for tailoring the interfacial adhesion or bonding for PEDOT:PSS nanosheets.

3.1. PEDOT:PSS/PEO aliquot preparation

Conductive-grade Poly (3,4-ethylenedioxythiophene)- poly (styrenesulfonate) (PEDOT:PSS, 1.7 wt.% in water, conductive grade) were obtained from Sigma Aldrich Canada without further modification. Poly(ethylene oxide) (PEO, MW = 500,000 gr/mol) were also brought in their white powder form from Sigma Aldrich Canada. The solvent used in the sample fabrication was Dimethyl Sulfoxide (DMSO), with a purity of

~99.9% (anhydrous, analytic grade) and was also obtained from Sigma Aldrich Canada.

First, PEO was dissolved in pure water and left overnight (the weight ratio of PEO to water was 1:3). The solid white powder adsorbed the water -albeit slowly- to form a translucent viscous white gel. An appropriate amount of pristine PEDOT:PSS was added with the PEO and homogenized with a high-speed homogenizer (MXBAOHENG, USA, head ⌀ 8 mm) at 12,000 rpm for five minutes per cycle, with a total of 12 cycles (with a cumulative time of 1 hour). The cycling method is intended to avoid overheating of the PEDOT:PSS that might lead to the breaking down of the polymeric bond. Hence, an additional water bath system was incorporated during the homogenization process. The temperature of the bath was kept around 5 degrees above the room temperature (25ºC).

The process was done entirely inside a well-ventilated fume hood. The environment was kept dim during the entire process, and PEDOT:PSS aliquots were covered with aluminum foil to avoid any light-induced breakdown processes.

An additional amount of DMSO was added to the aliquot prior to the homogenization. A variation of DMSO concentration ranges from 2 wt.% to 30 wt.% was incorporated into the PEDOT:PSS/PEO aliquot and subsequently homogenized together. PEO concentration was kept at a constant value to reduce variability across the groups and give identical viscosity for each group, which helped minimize errors in the adhesive force measurement that may be accounted for possible changes in the polymer sheet's rigidity.

3.2. Sample preparation and spin-coating

A cover glass (with a 12 mm ⌀) was used as the substrate, which was obtained from Thermo Fischer Canada (ON). Prior to fabricating the sample,

the glass was cleaned with distilled water, 95% v./v. ethanol and acetone in that order so as to remove any impurities that were present on the surface of the glass. PEDOT:PSS/PEO solution (either with or without DMSO) was transferred with a dropper to the cover glass, which was then spun at around 3,000 to 5,000 rpm for 30 seconds to make a flat and molecularly uniform film (spin-coating method with a Headway Spinner). A volumetrically precise amount of PEDOT:PSS was dropped each time to avoid producing ununiformed samples with different thicknesses. The rotation speed was then increased to a level about 30-50% higher than the base speed until the end of the process. The remaining water content on the resulting film was then evaporated.

The cover glass with the PEDOT:PSS/PEO coating (illustrated in Fig. 3.1) was then transferred to the hot plate and heated to about 135ºC for one hour (curing process) to remove any excess solvent and to ripen the polymeric sheet. PEDOT:PSS's content was estimated to be around 23.8 wt.% of the total weight that formed the resulting polymeric sheet.
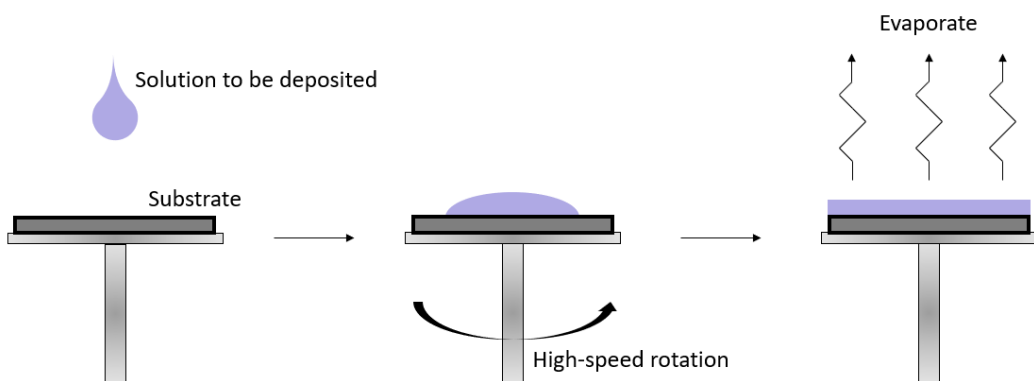
Figure 3.1. *Schematic diagram representing spin coating procedure.*

3.3. Characterization

The topography and surface potential were analyzed by employing the Kevin Probe Method using a Kelvin Probe Scanner. Gold was used as the reference with an established work function that is equal to 5.1 eV.

The adhesive force between the sample and the AFM tip (Si_3N_4) was measured using Bruker DIMENSION EDGE (Santa Barbara, United States) AFM Probe Machine. The cantilever was thermally tuned using the probe's built-in features. The thermal tuning was conducted by averaging the Brownian motion impetus imposed by the air toward the tips during an interval of time.

An optical microscope with a magnification of 100x was used to characterize the top-side morphology of the film. The morphological features of the film were analyzed based on real-time Optical Microscopy (OM) imaging.

The conductivity of the polymeric sheet was obtained using a standard method with a four-point probe system using a tungsten diode (Lucas Pro4 4000 sheet and bulk resistivity measurement system with Keithley 2601A sourcemeter) and confirmed with a further inspection using an AFM probe (Bruker NanoProbe, Santa Barbara CA, USA).

Nanoindentation was performed on the nanofilm with an Anton Paar NHT3 tribometer (Switzerland) with a triangular indenter head made from diamond. Depth offset adjustment (using a built-in protocol) was performed for each sample prior to each iteration. Height-depth curve was obtained for each indentation using a maximum imposed force of 25 mN, and Young's Modulus of each sample was thus determined.

The hardness of the material was obtained by dividing the max force exerted onto the surface by the contact area, which was extrapolated using the Oliver & Pharr's (OP) Method. Besides, Vickers Hardness was also measured.

3.4. Storage

PEDOT:PSS was stored in a fridge (Thermo Fischer, United States) all the time, under the optimal temperature of 2-5ºC. The container was wrapped with Aluminum foil to avoid any light-induced decay of the polymer. PEO was stored in a humidity-controlled container so as to prevent the polymer from absorbing any water vapor.

DMSO was stored in a chemically flammable container. A sterilized syringe (autoclaved) was used to transfer the DMSO out from the container and into the solution. The PEDOT:PSS spun-coated film was stored inside a biologically sterile-grade TCPS petri dish.

3.5. Statistical analyses

Statistical analyses were applied on the data using the Python Programing Language (PPL) basic pre-processing method, such as the module *numpy*, *scipy* and *pandas*, and the library *matplotlib.pyplot*. Further plotting was also carried using the Microsoft Excel's basic features.

3.6. Produced Aliquot and the PEDOT:PSS/PEO Spin-coated Polymeric Nanosheet

Following the vigorous homogenizing, the resulting aliquot is a dark blue and opaque solution that is more viscous than the original PEDOT:PSS solution. After the curing process, the thickness of the PEDOT:PSS/PEO nanosheet was approximated to be about 1000 nm. The produced nanosheet was observed to be thin and translucent.

The samples were observed and analyzed using an Optical Microscope (OM) and an Atomic Force Microscope (AFM). The surface height profile or topography of the samples was determined. There is no significant difference in the resulting AFM imaging between pristine PEDOT:PSS and DMSO-incorporated PEDOT:PSS. Fig. 3.2**B** presents AFM images of PEDOT:PSS films with and without DMSO.
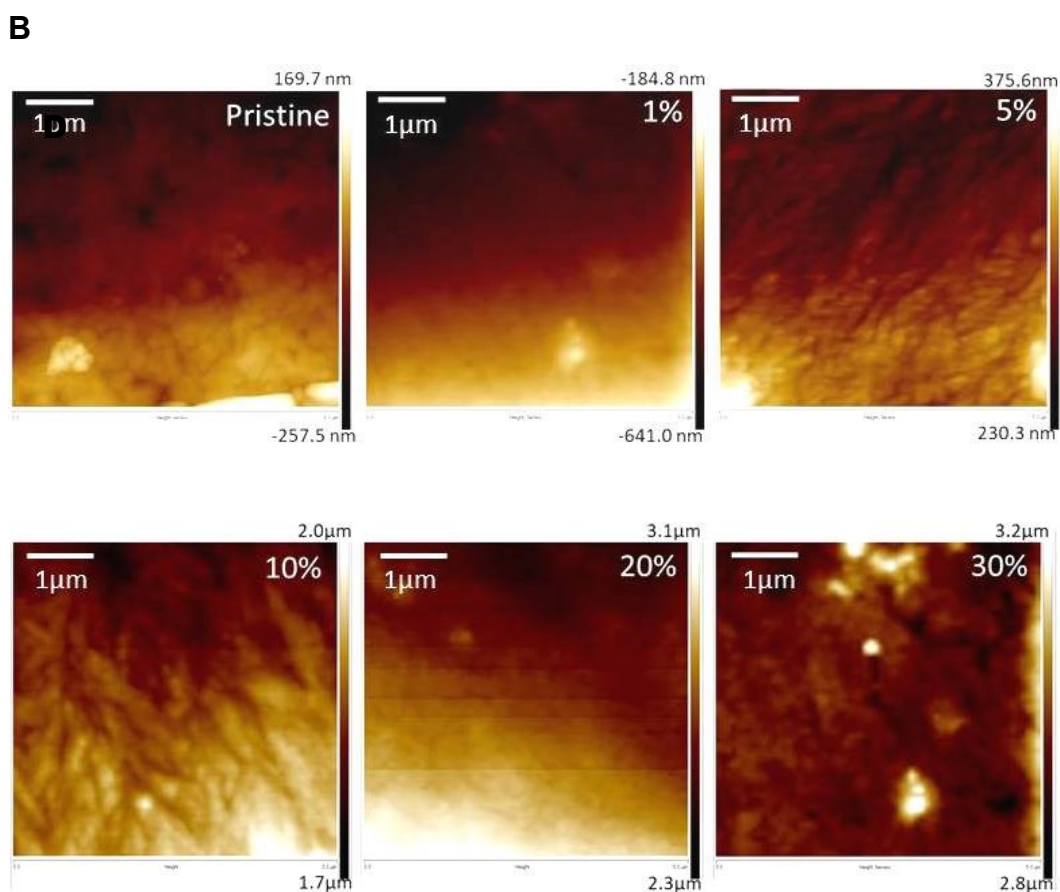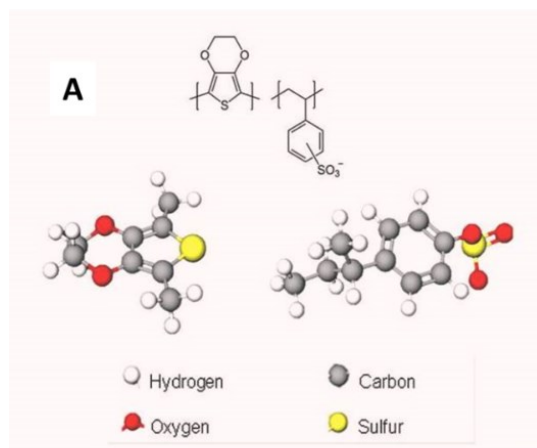
Figure 3.2. *A. PEDOT:PSS Chemical Structure and its 3D Representation (lower left: PEDOT; lower right: PSS); B. Closer views of spin coated PEDOT:PSS films with DMSO of different concentrations.*

No solid conclusions can be drawn by observing the AFM imaging alone. However, optical microscopic imaging of the corresponding PEDOT:PSS nanosheet showed distinctive morphological features across the nanosheets with differing DMSO contents. The optical images are presented later in Fig. 3.7 with relevant analysis regarding the effect of DMSO on the sheet's morphologies.

3.7. Conductivity analysis

The electrical resistivity of the sheets was measured (Fig. 3.3(a)) using a standard Four-Point Probes with an applied current that was automatically determined by setting an iterative range from 0 A to 0.5 mA. The apparatus determined the optimal current and was subsequently used to measure the resistivity of the polymeric sheets. Five different points on each sample were measured to obtain an average value and its variations.

(a)

(b)
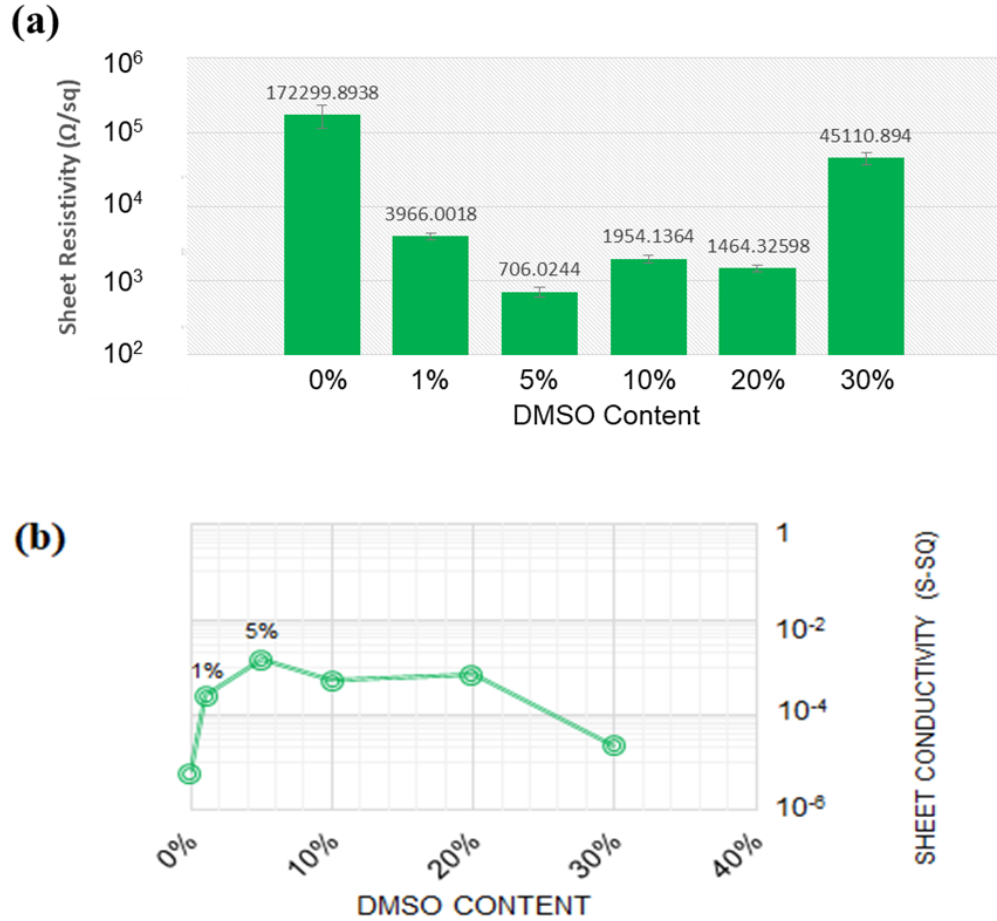
Figure 3.3. *(a) Sheets' electrical resistivity (in Ω/sqcm) as measured using the Four-Point Probing Method; (b) Sheets' conductivity (in S-sqcm) obtained from the measured electrical resistivity.*

Corresponding electrical conductivity of the sheets was calculated [Fig. 3.3(b)], which is the inverse of the resistivity [91-92].

$$\sigma = \frac{1}{\rho} \tag{3-1}$$

where σ is the sheet's conductivity (S·cm²), and ρ is the sheet's resistivity (Ω/cm²). Both Figures 3.3 (a) and (b) are plotted in a logarithmic scale. As shown, the conductivity is highly ameliorated with a small addition of 1%

and 5% (wt./wt.) DMSO into the aliquot. While the pristine group has a low conductivity, the addition of DMSO considerably increases the conductivity of the polymeric sheet. However, as the DMSO content increases to a certain level around 10%, the sheet conductivity gradually decreases, rendering the nanosheet less conductive.

3.8. Adhesive force measurement

The adhesion behavior of the samples was analyzed using AFM (Bruker-Dimension Edge). Fig. 3.4 illustrates the adhesive force between the AFM Si_3N_4 tip and the samples. As shown, the DMSO increases the adhesive force, where 5% DMSO group corresponds to the maximum increase in adhesive force, which was calculated to be 35.8% higher than the original pristine group's value.

The adhesive force then decreases as the DMSO content continuously increases, plateauing after the DMSO value ranges 10-20%. As the DMSO concentration reaches 30%, the adhesive force significantly decreases, even lower than the pristine group.
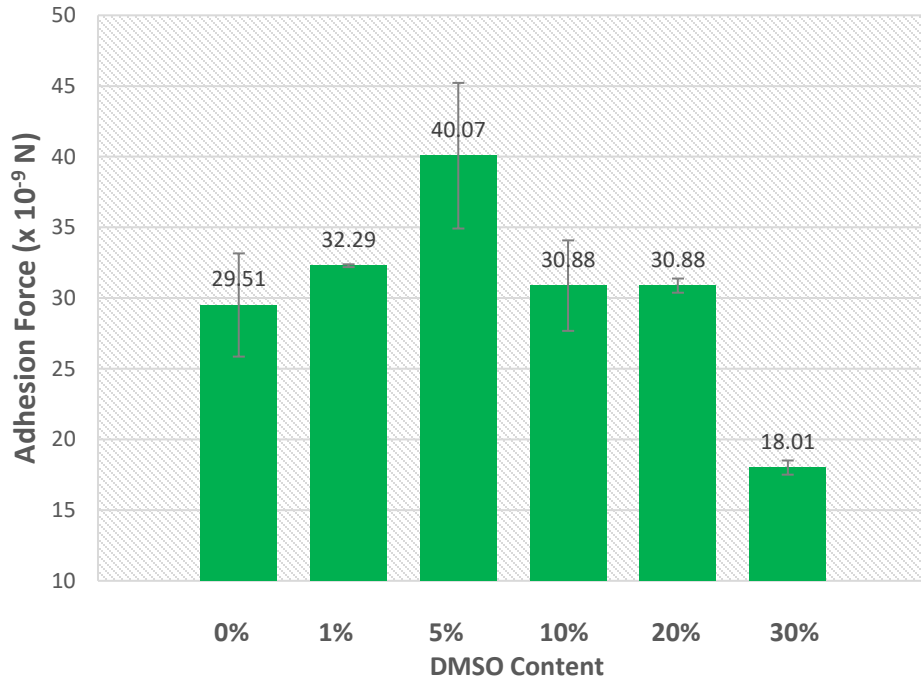
Figure 3.4. *The adhesive force was obtained for each group of the samples.*

3.9. Electron Work Function (EWF) measurement

The Electron Work Function of the samples was determined using a Kelvin Probe Scanner (KP Technology-United Kingdom) with pure gold as reference (WF ≈ 5.1 eV). EWF is the minimum required energy to move an electron at the Fermi level from inside a solid to its surface [84]. EWF is related to the electron activity and relates to the adhesive force, as discussed later. Results of the EWF measurement are presented in Fig. 3.5.

It should be noted that EWF is the function of material surface, and not that of the bulk of the material.
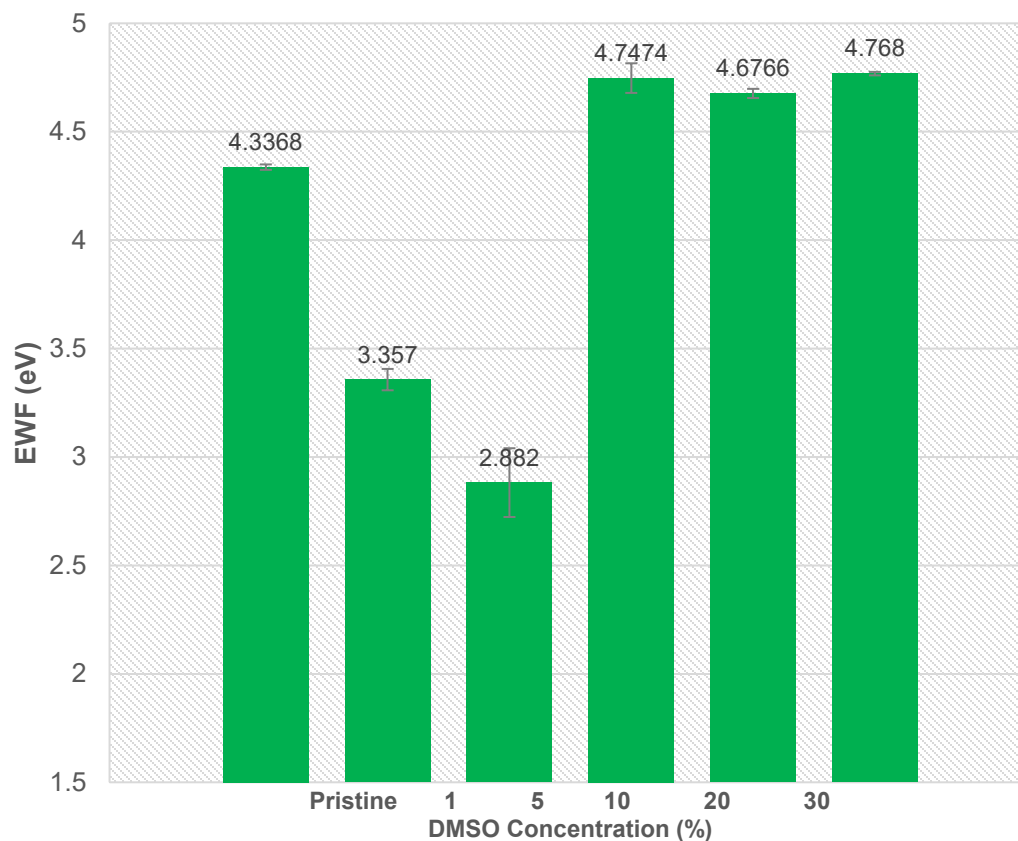
Figure 3.5. *EWFs of PEDOT:PSS/PEO with different concentrations of DMSO (%).*

3.10. Young's Modulus and hardness measurement

Young's Modulus and hardness of the PEDOT:PSS/PEO sheets with different DMSO amounts added to the aliquot were measured. Results of the measurements are illustrated in Fig. 3.6. As shown, both Young's Modulus and hardness of the sheet are not changed with the DMSO doping up to about 20 wt.%. When the doping reached 30 wt.%, the Young's Modulus and hardness were severely affected. From the observation using an optical microscope, it was established that by 30 wt.% DMSO doping, the ability of PEDOT:PSS/PEO to form a continuous nanofilm was primarily

degraded. Agglomeration of the film took place, creating tiny individual bubbles across the sample as illustrated in Fig. 3.7.

With this in mind, the decreases in Young's Modulus (as measured with a nano indenter) and hardness in the 30 wt.% group became understandable.
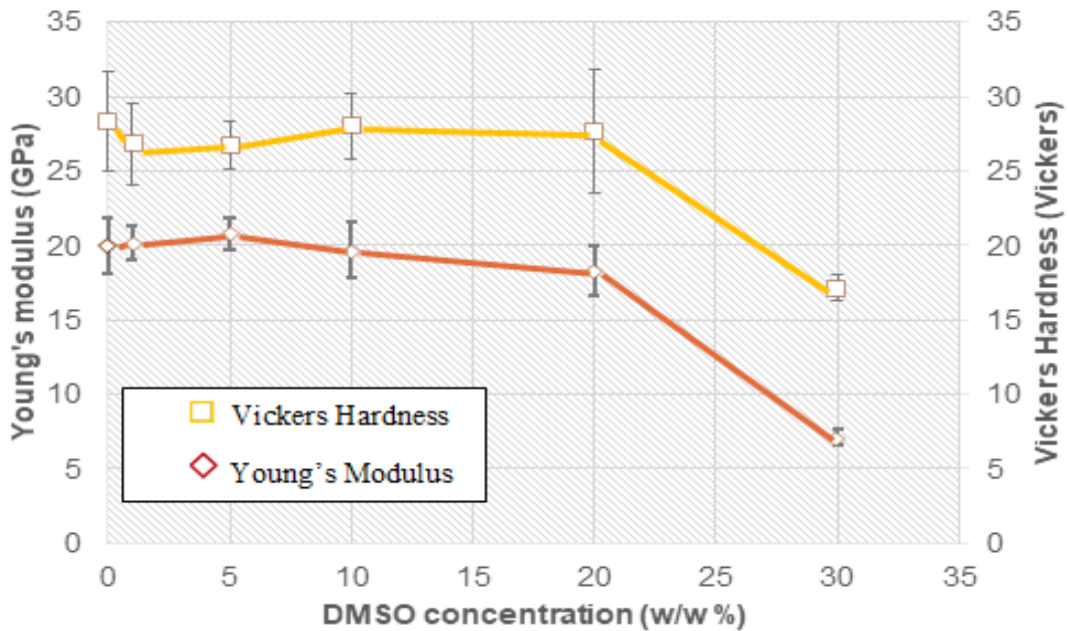
Figure 3.6. *Young's Modulus and hardness of the PEDOT:PSS/PEO film versus the DMSO concentration.*
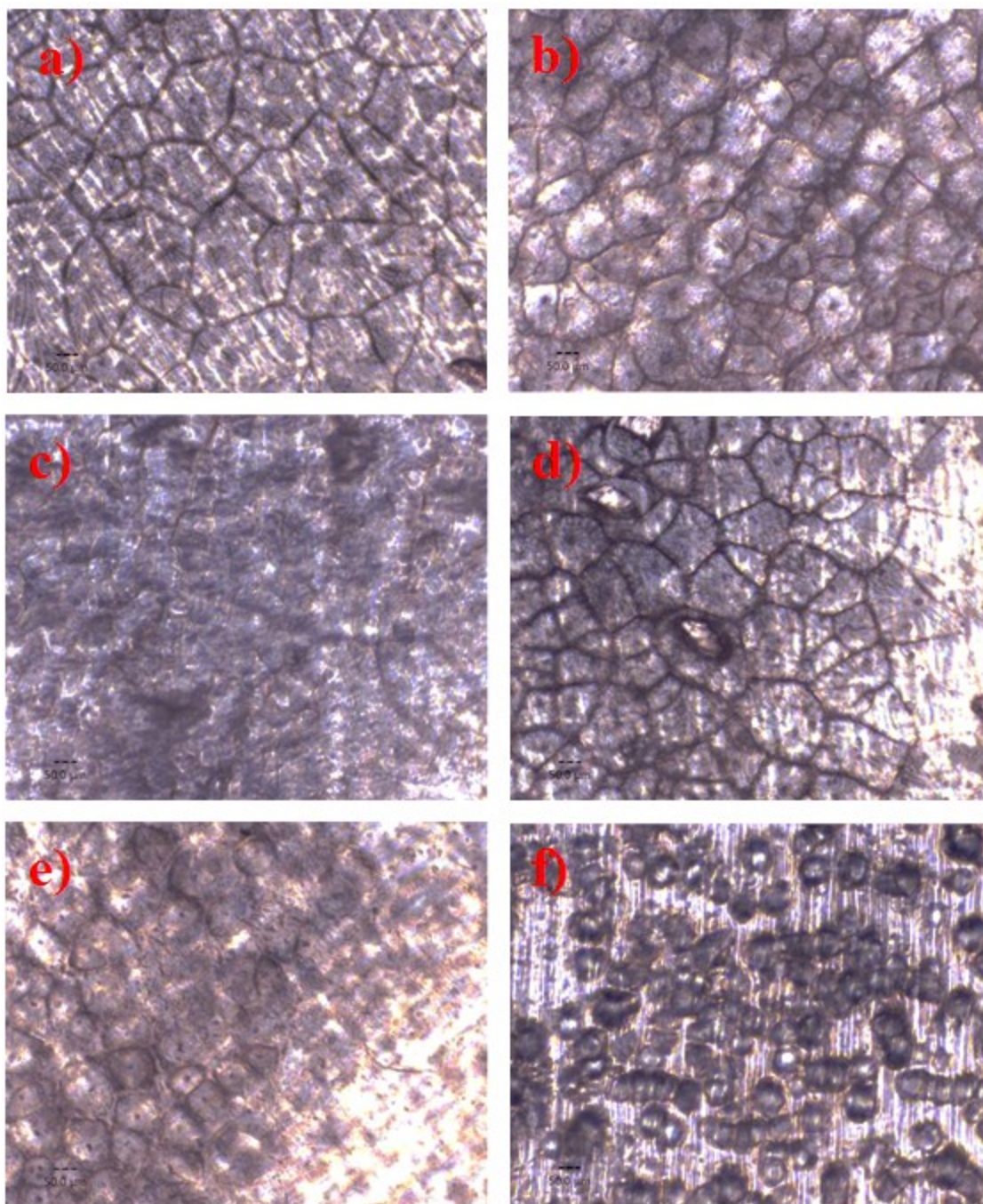
Figure 3.7. *Optical microscope imaging for PEDOT:PSS/PEO: a) Pristine; b) 1 wt.% DMSO; c) 5 wt.% DMSO; d) 10 wt.% DMSO; e) 20 wt.% DMSO; f) 30 wt.% DMSO.*

3.11. Discussions

With the introduction of DMSO into the aliquot, the PSS on the surface of the nanofilm is washed away, changing the ratio of the PEDOT to PSS. The chief reason this happened is that DMSO contains a strong polar group that interacts strongly with the PSS's sulfonic acid group, coupled with its ability to diffuse into the PSS shell and prefers the phase separation from hydrophobic PEDOT [61].

The increase in PEDOT:PSS's conductivity by incorporating DMSO is a well-known fact, which is ascribed to the fact that DMSO and water act as cosolvents (a solvent that is used in conjunction with another solvent) to solvate the PEDOT:PSS. The preferential solvation induces the phase separation of the insulative PSS chain from the PEDOT:PSS main backbone, followed by an aggregation of some segments of the PSS and the overall conformational change of the polymer spatial arrangement from a coiled form to a linear form [75].

Lower DMSO concentrations may not be enough to trigger any sufficient conformational changes. The 5% DMSO concentration results in the highest conductivity increase. However, suppose the DMSO concentrations exceed a certain level. In that case, the polymer integrity will excessively deteriorate since DMSO dominates the solution and thus hinders the formation of any continuous PEDOT:PSS/PEO network.

The DMSO can induce the rearrangement of the PEDOT:PSS chain, increasing the alignment of the molecular π-bonds. This reduces the 'hopping' distance of the electron/hole pairs, leading to an increase in the film's conductivity. Hopping distance is the distance a charge must be transported in order for it to be dispositioned from one point in space to another point at certain energy levels. According to Nardes, *et al.* [82], the hopping distance of an electron in a PEDOT-PSS system is about 60-90 nm. The conductivity of a general organic material can be represented as:

45

$$\sigma = \sigma_0 \, e^{\left[-\left(\frac{T_0}{T}\right)^a\right]} \tag{3-2}$$

$$a = \frac{1}{(1+D)} \tag{3-3}$$

$$T_0 = \frac{4}{k_B N(E_F) \xi'} \tag{3-4}$$

where σ is the conductivity, σ_0 the conductivity of the organic material at infinite temperature, T_0 the characteristic temperature, D the dimensionality of the system (i.e., $D = 3$ for a 3-D system), k_B is the Boltzmann constant, $N(E_F)$ the density of localized states at Fermi level (eV^{-1} m^{-3}), and ξ' represents the effective localization length (m). The above function is applicable to PEDOT:PSS system.

According to the model, increasing the density of state (DOS) at the Fermi level and the localization length will increase the overall conductivity. The decrease in T_0 can thus be likened to the reduction of the energy barrier needed for the charge transport across the conductive body, which should also be reflected by a lowered work function (EWF) which can also be associated with an elevated degree of freedom for electrons to move across the 3D space within the confinement of the nanosheets.

This is corroborated by our experimental observation of the relation between EWF and electrical resistivity, as illustrated by Fig. 3.8, in which data from Figs. 3.3 to 3.5 are plotted together to reveal their relationships more clearly. As shown here, a lower WF corresponds to lower resistivity and higher conductivity.

The work by Nardes, *et al.* [82] has demonstrated that by using 2.5 wt.% sorbitol as the solvent, the $N(E_F)$ and ξ' of PEDOT:PSS ($1.4 \pm 0.2 \times 10^{17}$ eV^{-1}·cm^{-3} and 8.2 ± 0.5 nm respectively) jumped to $1.9 \pm 0.4 \times 10^{18}$ eV^{-1}·cm^{-3} and 33 ± 2 nm respectively. It is confirmed that the increase of $N(E_F)$ and ξ' by the sorbitol treatment also decreases the T_0 of the PEDOT:PSS (refer to eq. (3-4)).
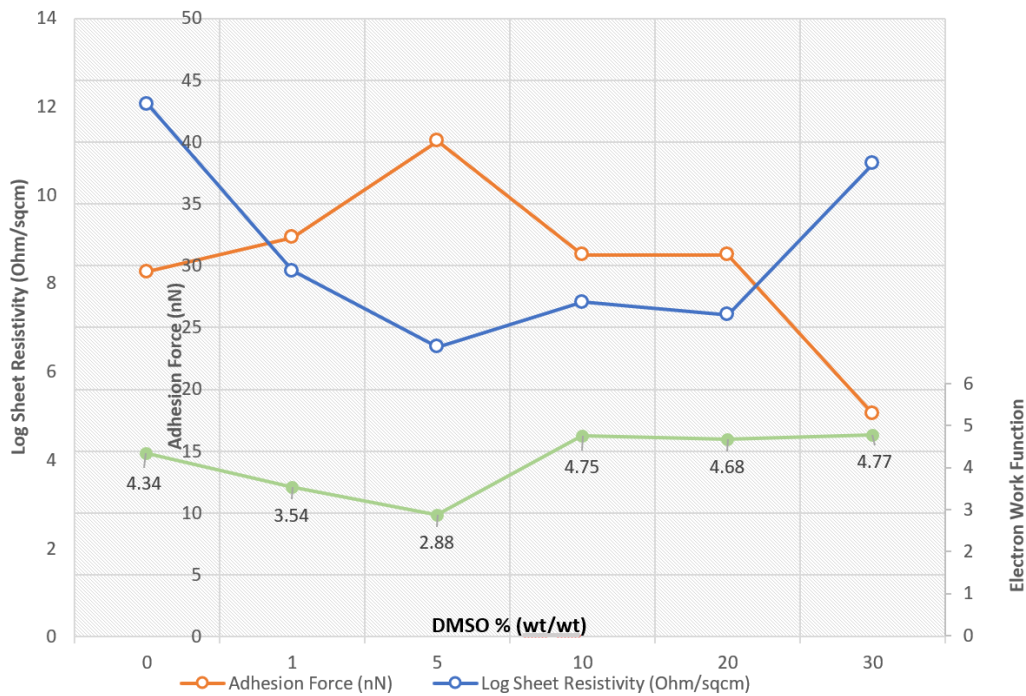
Figure 3.8. *Electrical resistivity, EWF, and adhesion force against %DMSO.*

The increased conductivity is a direct indication that electrons have higher freedom to move, which helps to increase the interaction or bonding with the Si_3N_4 AFM tip. The EWF for Si_3N_4 is reported to be 5.3 eV [85]. The interactions between different types of materials such as ceramics-polymer are generally weak. A previous study (Li, *et al.* [71]) on ceramics-metal pair shows that the interaction at interface comes from the formation of a dipole layer induced by the difference in Electron Work Function between the materials in contact, which is also influenced by the freedom of electrons (as illustrated by Fig 3.9). Fig. 3.10 illustrates the situation when the two materials are in contact.
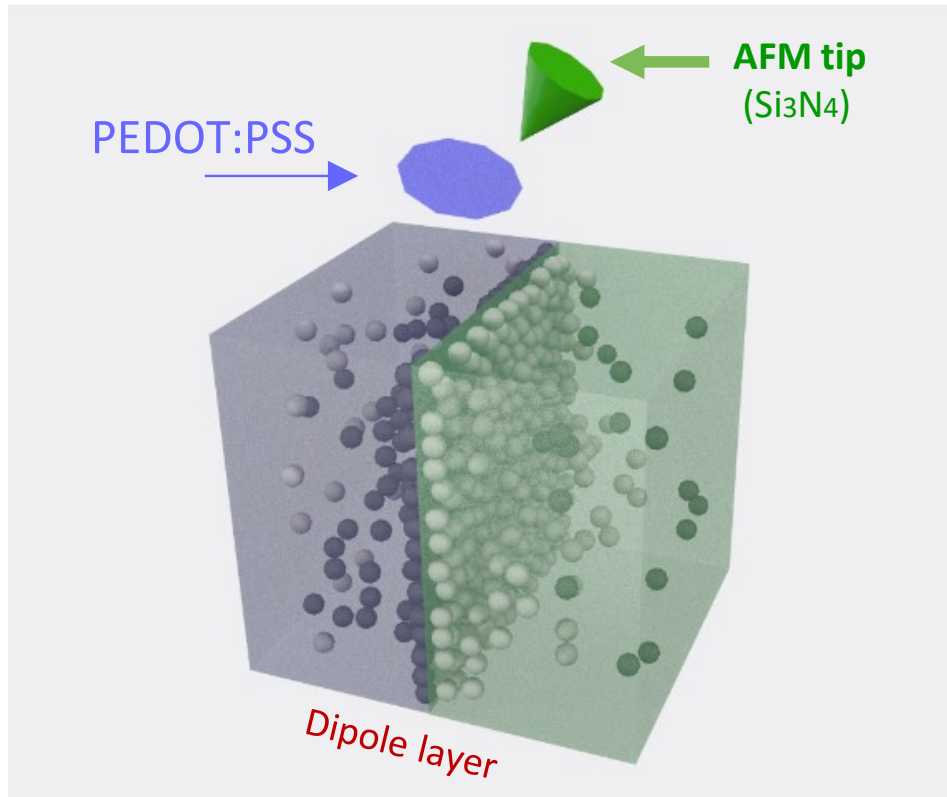
Figure 3.9. *The schematics representation of the dipole-dipole layer formed across the interface of PEDOT:PSS/PEO polymeric nanosheet with AFM tip/cantilever modified with Si_3N_4.*

As shown in Fig. 3.10(a), when the two different types of material are in contact with minor or without atomic diffusion, their Fermi levels at the interface would converge, thus developing a potential difference, $\Delta V = (\varphi_B - \varphi_A)/e_0$, where e_0 is the unit charge [16]. Under the potential difference, electrons will move from the material with a lower work function (φ_A) to the one with a high work function (φ_B) to achieve equilibrium in the system. As a result, a dipole layer forms at the A/B interface, as Fig. 3.10 (b) illustrates, which induces the interfacial interaction or interfacial bonding.
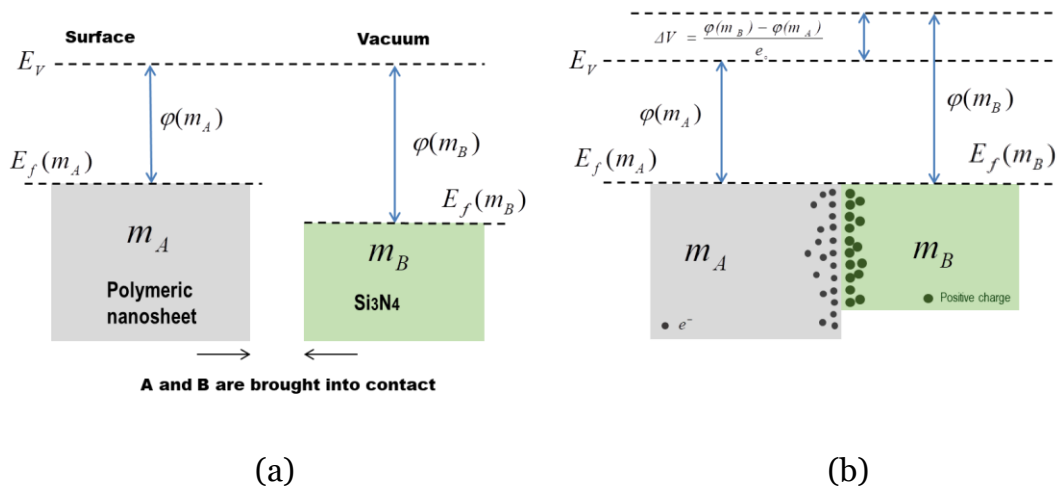
Figure 3.10. *(a) when material A having a low work function and B with a higher work function are in contact, (b) electrons move towards the high-work function site, driven by the potential difference, ΔV. As a result, a dipole layer is established at the interface, which acts as a barrier to electron migration and develops interfacial bonding.*

Electrons come from the interior of the bulk material, driven by the Contact Potential Difference (CPD) as the driving force. The mobile charge can come from many factors, including defects in the material, impurities, *et cetera*. However, if the materials are perfectly non-conductive or electrons are fully localized, electrons are unable to migrate, and the dipole layer cannot be developed. As a result, no interfacial bonding can be established. Thus, the difference in work function and the degree of electron freedom should affect the interfacial bonding.

The former is related to the driving force or the tendency to establish interfacial bonding, while the latter determines if the bonding can be established. Based on this mechanism of the adhesive force model, the measured variations in the adhesive force of the PEDOT:PSS/PEO nanofilm containing different amounts of DMSO (Fig. 3.7) becomes understandable.

As Fig. 3.8 or Figs. 3.3 and 3.5 illustrate, the conductivity of the nanofilm increases as more DMSO is added, accompanied by a subsequent decrease in EWF. It should be noted that DMSO doping decreases the insulating

barrier thickness of PSS between conducting grains. On the other hand, the increased electron freedom facilitates the charge movement to establish the dipole layer when the nanofilm is in contact with the Si_3N_4 tip. Subsequently, the decrease in EWF of the nanofilm enlarges the difference in EWF between Si_3N_4 and the nanofilm, which increases the potential difference at the interface and thus provides a more significant driving force for developing the dipole layer; ergo, the adhesive force increases as shown in Figs. 3.4 and 3.8.

However, with an extreme addition of DMSO, the situation is reversed. The conductivity decreases along with an increase in EWF as more DMSO is added into the system, reducing the adhesive force. As the concentration of the DMSO is increased to an extreme degree (i.e., until 30 wt./wt. %), the system shows the most inadequate adhesive profile along with the formation of intensive bubbles, as Fig. 3.7 illustrates.

As mentioned earlier, excessive DMSO deteriorates the polymer integrity and restricts the intramolecular interaction between polymers, resulting in clustered polymeric bubbles. This renders the polymeric nanosheet's conductivity highly compromised since the polymeric sheet with poor structural integrity cannot conduct electrons effectively, if at all.

In the Figs. 3.7 (a)-(f), the morphology of the PEDOT:PSS nanofilm is shown for different DMSO concentrations. Cracks or bubbles can be seen on the films after the heat treatment or curing, which was performed to remove any excess solvents and ripen the polymeric sheet (see **Sample preparation and spin-coating**). However, the film with 5% DMSO does not show either cracks or bubbles, thus demonstrating the highest structural integrity. This is a fact that has been established by a previous study [87]. Furthermore, Cruz-cruz, *et al.* [86] reported that the optimal concentration of DMSO doping for PEDOT:PSS nanofilm could achieve the highest conductivity at 17 wt./wt. %. In our case, the best overall performance is reached with a concentration of DMSO equals 5 wt.%. DMSO interferes highly with the material; therefore, any excessive concentration of DMSO will impose negative repercussions to the nanofilm

itself. With a very high DMSO concentration, the PEDOT:PSS film may start to have a pronounced grain separation, leading to an enormous spatial gap of conducting grains. As the conductivity decreases, the Electron Work Function is increased. This is understandable, as the electron is even more reluctant to move, requiring more energy to excite the electron and bring it down to the vacuum level.

From Fig. 3.6, one can infer that adding DMSO into the PEDOT:PSS/PEO aliquot as a solvent treatment does not alter the mechanical and tribological properties of the resulting nanofilm as long as the DMSO concentration is below the 20 wt.% threshold. Thus, the measured increase in adhesive force with DMSO can be attributed solely to the increased dipole-dipole interaction at the interface of Si_3N_4 tip and the nanofilm, excluding the influence of variations in tip/contact area caused by possible changes in the mechanical strength of the nanofilm.

Chapter IV:
Pure Metal's Adhesion Profile with Si$_3$N$_4$ Surface

In this chapter, the results obtained from a study on interfacial adhesion between silicon nitride and several metals are presented and elaborated. The preceding theory that may juxtapose or complement the study is also incorporated and further debated.

This study is aimed to provide a theoretical model that is quantitative and analytical in nature in response to the observation made from the initial research laid out in Chapter III, which guarantees that increased work function may play a role in increasing the adhesive force between the polymeric nanosheet and silicon nitride probe. Using pure metals as samples may provide a more theoretical insight into the effect of adhesion arising from electrostatic potential (*electroadhesion*).

4.1. Sample preparation

Seven pure metals (Iron, Chromium, Manganese, Copper, Titanium, Vanadium, Silicon) were acquired from the suppliers (Sigma Aldrich, ON, Canada) without further modifications. The average size of metallic samples was 1.5 cm x 1.5 cm x 0.5 cm.

The samples were polished using a metal polisher NANO-1000S Grinder-Polisher (Pace Technologies, United States). The samples were ground using sandpapers range from the roughest grid until the smoothest

grid (50, 100, 200, 400, 800, 1000) subsequently in that order. The samples were then polished using 1 μm Alumina powder (Al_2O_3) at 1000 rpm on a polisher cloth with the suitable amount of water introduced during the polishing (the water flow rate was approximately 1 cm^3/s). The samples were then cleaned with laboratory-grade DI water followed by a 75% isopropyl alcohol (C_3H_7OH) treatment (Sigma Aldrich, ON Canada).

4.2. Characterization

The metals' Electron Work Function (EWF) was measured with Kelvin Probe Scanner (KP Tech, UK). The measurement was repeated several times and was performed on five different spots for each sample. The average value of EWF was obtained from the repeated measures.

Tests were performed to correlate the material's EWF with adhesive forces (F_{Ad}) with a Si_3N_4 probe. The F_{Ad} with the seven pure (~99.5%) metals (Fe, Cr, Mn, Cu, Ti, V, and Si) was measured using a Dimension EDGE AFM (Bruker, USA). The Si_3N_4 probe EWF was already known as 5.30 eV. The probing was done on five different spots, and the average of those five values was obtained.

4.3. Storage

The samples were then stored inside a vacuum chamber to minimize any air-induced oxidation and prevent any contamination. This step is deemed necessary since oxidation may create a metal-oxide layer on the surface of the metals, which then could affect the surface properties, conductivities, and Electron Work Function (EWF) values.

4.4. Calculation and data analyses

The obtained data were further processed using the Python Programing Language (PPL) basic pre-processing, using the module *numpy*, *scipy* and *pandas*, and the library *matplotlib.pyplot*. Further plotting also carried on using the Microsoft Excel basic features. Furthermore, the calculations of theoretical F_{Ad} were carried out using *Wolfram Mathematica*.

The 3D models were built using the modeling-rendering software *Vectary*. The 3D models presented in this thesis, unless otherwise mentioned, were modeled by using the abovementioned software.

4.5. Observations

The metals' measured EWFs, and adhesive forces with Si_3N_4 are illustrated in Fig. 4.1, and values are given in Table 4.1, respectively.
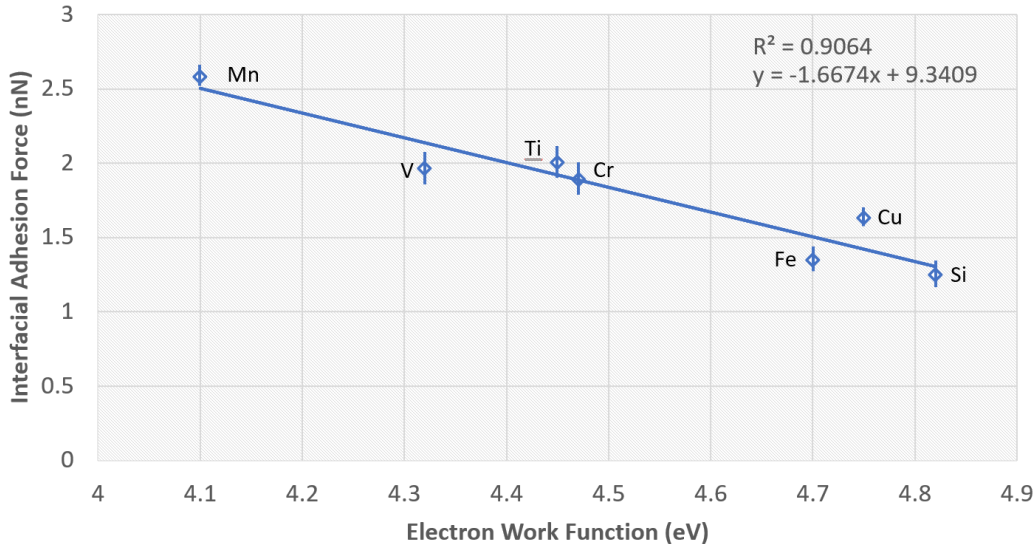
Figure 4.1. *The interfacial adhesive force between the metal surface and Si_3N_4 tip (in nN) plotted against the EWFs (eV) of the metals*

54

Table 4.1. *EWFs of the metals under study and their interfacial adhesive forces with Si_3N_4.*

Elements	φ (eV)	F_{Ad} (measured) (nN = 10^{-9} N)
Silicon (Si)	4.82 ± 0.05	1.251 ± 0.15
Copper (Cu)	4.75 ± 0.10	1.632 ± 0.11
Iron (Fe)	4.70 ± 0.06	1.354 ± 0.18
Chromium (Cr)	4.47 ± 0.08	1.888 ± 0.22
Titanium (Ti)	4.45 ± 0.07	2.006 ± 0.20
Vanadium (V)	4.32 ± 0.07	1.963 ± 0.22
Manganese (Mn)	4.10 ± 0.06	2.587 ± 0.16

4.6. Theoretical expositions

When two materials (A and B) are brought together into contact, a charge transfer will take place, forming an electrical double layer [93-95] until the charge distribution stabilizes and reaches an equilibrium [13, 93]. As illustrated in Fig. 4.2, the Fermi energies of the two materials must converge at the interface [13, 96-97]. Electrons then move from the material having a low work function $\varphi(m_A)$ to that having a higher work function $\varphi(m_B)$. A potential difference (ΔV) is thus established at the interface of the two materials, which is determined by the difference in work function between the two materials [22],

$$\Delta V(m_A | m_B) = \frac{\varphi(m_B) - \varphi(m_A)}{e} \tag{4-1}$$

This potential difference generates an opposite electrical field to stop continuous charge movement and thus establishes a dipole layer at the interface.
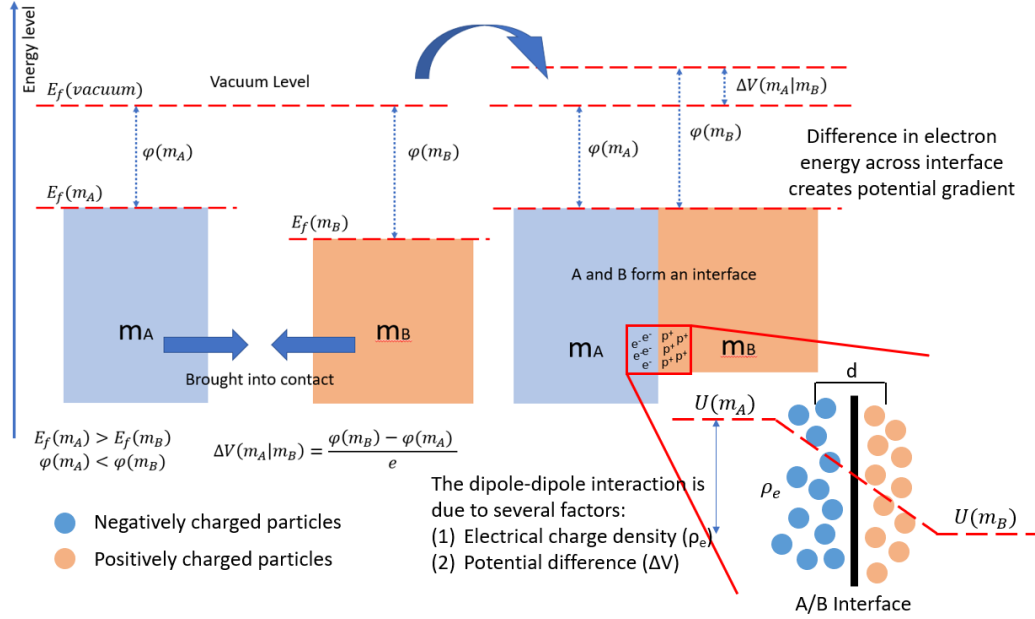
Figure 4.2. *The schematics of an electrical double layer (EDL) formation across interface due to the difference in Electron Work Functions (EWF) between two different materials, A and B.*

The potential difference can also be correlated to the energy of the electrons (U) [93]:

$$U = \frac{1}{2} E \rho_e d = \frac{1}{2} \Delta V(m_A | m_B) \rho_e \tag{4-2}$$

where E is the electrical field, ρ_e denotes the charge density of the dipole layer across the interface, and d is the charge separation distance over the dipole layer. According to the Gaussian's Law, E is defined as [98]:

$$\nabla \cdot E = \frac{\rho_e}{\varepsilon_0} \qquad\qquad (4-3)$$

where E is the electrical field in vacuum, and ε (for air ~ 1.0) and ε₀ (8.8541878176 x 10⁻¹² F/m) are the relative permittivity and absolute permittivity in a vacuum, respectively. The attractive electrostatic pressure P_A in a non-vacuum medium is given and can be correlated to the adhesive force F_{Ad} [93, 99-100]:

$$P_A = \frac{1}{2} E \rho_e = \frac{1}{2d^2} (\Delta V(m_A|m_B))^2 \varepsilon \varepsilon_0 = \sum_{i=1}^{n} \gamma_i F_{Ad_i}^{n-i} \qquad\qquad (4-4)$$

The last term corresponds to the multi-degree approximation of the measured adhesive force using an AFM (Taylor's expansion). In this study, however, we show that one- or two-degree(s) polynomial (i.e., linear approximation, quadratic approximation) yields good fitting on the obtained data.

Analytically, we can obtain the force from eq. (4-4) by integrating P_A to the area dA:

$$F = \int \frac{1}{2d^2} (\Delta V(m_A|m_B))^2 \varepsilon \varepsilon_0 \hat{z} \, dA \qquad\qquad (4-5)$$

where $\hat{z}$ represents the perpendicular axis-vector of the two separated bodies. For two planar surfaces with an arbitrary contact area of A_c:

$$F_{Ad} = \frac{1}{2d^2} (\Delta V(m_A|m_B))^2 \varepsilon \varepsilon_0 A_c = \frac{1}{2d^2} \varepsilon \varepsilon_0 \left(\frac{\varphi(m_B) - \varphi(m_A)}{e} \right)^2 A_c \qquad (4-6)$$

where e is the unit/elementary charge (1.60218 x 10⁻¹⁹ coulombs). The unit of F_{Ad} is Newton (kg·m·s⁻²). The charge separation distance (*d*) has been shown to be typically ~1 nm for several materials with Si_3N_4 [93].

We may use the extrapolation method to find the approximate charge separation distance d using two other readily available physical properties: the bulk electron density ($\rho_{e\text{-bulk}}$) and electrical conductivity (σ_{bulk}). The conductivity influences the charge density at the interface [13], which affects the strength of electrostatic interaction at the dipole layer and affects the interfacial adhesive profile. The conductivity can therefore be related to the charges' freedom of movement. Materials having more charges/electrons with higher movement freedom should be more prone to have more charges/electrons accumulated at the interface under identical potential differences.

As the charges build up, the accumulation of charges at the interface and the separation length between the charges across the interface are influenced by their availability and movement freedom, closely entangled to the bulk charge density and conductivity. We may introduce a new term:

$$d \rightarrow f[\rho_{e-bulk}(m_A), \widetilde{\sigma}(m_A), \rho_{e-bulk}(m_B), \widetilde{\sigma}(m_B)] \qquad (4-7)$$

$$\widetilde{\sigma}(m_A) = \frac{\sigma(m_A)}{\sigma(Ag)} \quad ; \quad \widetilde{\sigma}(m_B) = \frac{\sigma(m_B)}{\sigma(Ag)} \qquad (4-8)$$

where $\tilde{\sigma}$ is a prescribed relative conductivity (unitless), defined as the ratio of the said material's conductivity to that of pure silver as a hypothetical reference (Ag, $\sigma(Ag) = 63 \times 10^6$ S/m). In the present study on the adhesive forces between silicon nitride and several metals, the counterpart for all the metals is the same, i.e., silicon nitride. Thus, the charge separation distance is represented by $d= f[\rho_{e-bulk}(m_A), \tilde{\sigma}(m_A), C]$, which is a function of the relative conductivity and bulk charge density of the metal in contact with Si_3N_4, while C reflects $\rho_{e-bulk}(m_B)$ and $\widetilde{\sigma}(m_B)$ of Si_3N_4 ($m_B = Si_3N_4$), which is constant throughout all tests. Eq. (4-6) may thus be turned into an alternative form:

$$F_{Ad} = \frac{1}{2d^2} \varepsilon \varepsilon_0 \left(\frac{\varphi(m_B) - \varphi(m_A)}{e} \right)^2 A_c$$

$$= \frac{\varepsilon \varepsilon_0 \, A_c}{2\{f[\rho_{e-bulk}(m_A), \tilde{\sigma}(m_A), C]\}^2} \left(\frac{\varphi(m_B) - \varphi(m_A)}{e} \right)^2 \qquad (4-9)$$

To determine the form of $d = f(x_i)$, where x_i represents different items, we performed the following calculations in combination with experimental data analysis. The method used to calculate metal's ρ_{e-bulk} is eq.(4-10), invoking the following relationship involving mass density (ρ), Avogadro's Number N_{Av} (6.0221409 x 10²³), atomic valence number (Σ_{val}, i.e., $\Sigma_{val}(Si) = 4$), and atomic mass (A_r, i.e., for Si: $Si_{14}^{28.0855}$). Such a relationship shown in eq. (4-10) is relatively straightforward and will not be elaborated further, but be described below as:

$$\rho_{e-bulk}(m_A) = \left[\frac{\rho N_{Av} \Sigma_{val}}{A_r} \right] (m_A) \qquad (4-10)$$

Substituting eq. (4-10) to eq. (4-9) yields:

$$F_{Ad} = \frac{\varepsilon \varepsilon_0 \, A_c}{2\{f[\left[\frac{\rho N_{Av} \Sigma_{val}}{A_r} \right](m_A), \tilde{\sigma}(m_A), C]\}^2} \left(\frac{\varphi(m_B) - \varphi(m_A)}{e} \right)^2 \qquad (4-11)$$

4.7. Results and discussions

Through data analysis, we can see that by using $d \sim 1$ nm to calculate F_{Ad} using eq. (4-6) alone and without involving eqs. (4-7) − (4-11), we can achieve a reasonable convergence between the calculated values with the experimentally measured values for individual materials and data points in terms of the numerical order (see Fig. 4.3 and Table 4.2), thus corroborating

the theoretical soundness of the above model. The contact area was analytically calculated as the area of the half-sphere of the silicon nitride tip attached to the AFM cantilever, with a known diameter of 20 nm. Some errors are expected since we use the separation length $d \sim 1$ nm for all the metals, which is not the case in real-world applications (i.e., different materials have different values of d based on their ρ_e).

Table 4.2. *Adhesion force as calculated with the proposed model.*

Elements	F_{Ad} (measured) (nN)	F_{Ad} (calculated) with d ~ 1nm (nN)	Deviation (nN)	$\tilde{\sigma}$	ρ_{e-bulk} $(10^{28}/m^3)$	d calc. (nm)
Iron (Fe)	1.354 ± 0.18	1.000	+0.354	14.6	16.98	0.859
Chromium (Cr)	1.888 ± 0.22	1.914	-0.026	16.0	49.68	1.006
Manganese (Mn)	2.587 ± 0.16	4.002	-1.415	15.8	55.69	1.24
Copper (Cu)	1.632 ± 0.11	0.8406	+0.7914	96.5	8.45	0.718
Titanium (Ti)	2.006 ± 0.20	2.001	+0.005	13.7	18.10	0.998
Vanadium (V)	1.963 ± 0.22	2.669	-0.706	5.0	28.85	1.166
Silicon (Si)	1.251 ± 0.15	0.6403	+0.6107	20.5	19.98	0.715
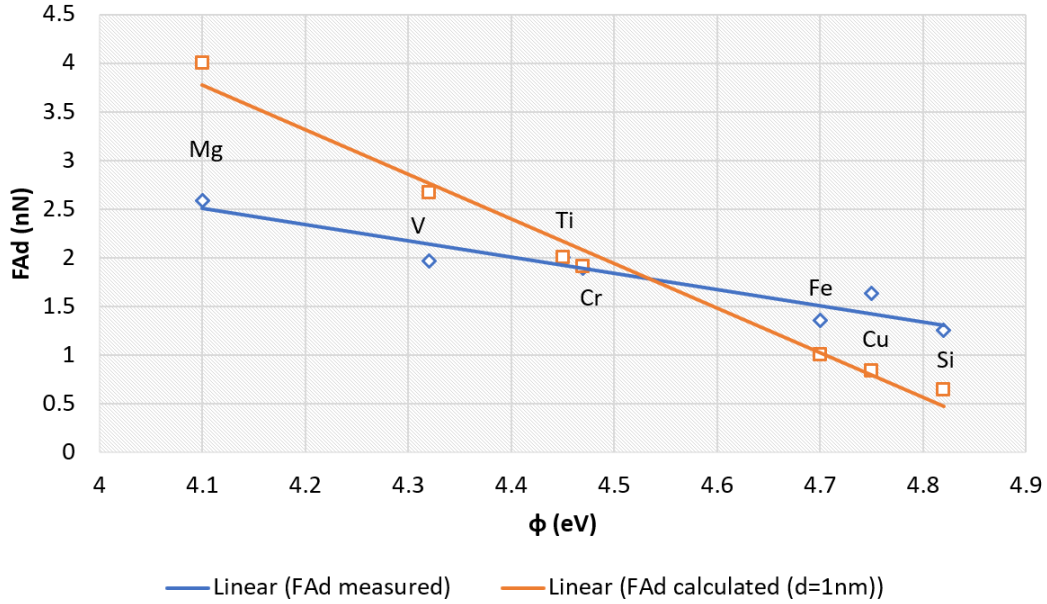
Figure 4.3. *The interfacial adhesive force between the metal surface and Si₃N₄ tip (in nN) plotted against the EWFs (eV) of the metals, calculated using eq. (4-6).*

Using the theoretically estimated values of $d \sim 1$ nm for all the metals, it is worth noting that the theoretically estimated values are in the same order as those from experimental measurements (estimated values: 1.0-4.0 nN; experimental values: 1.2-2.6 nN), with a preserved trend. The existing discrepancy should be related to the variation in the separation distance d, influenced by the conductivity and charge density as shown by eqs. (4-9) – (4-11). Both higher conductivity and charge density favors the charge accumulation at the interface. However, a physical constraint exists with the dipole-dipole interaction. When the electrostatic pressure exceeds a certain level, the dipole-dipole moment will reach a stagnant value due to charge saturation or over-accumulation adjacent to the interface. As a result, the separation length would increase. Based on the above analysis and discussion, we take $d = f[\rho_{e-bulk}(m_A), \widetilde{\sigma}(m_A), C]$ as an approximation function of the product of relative conductivity of a particular metal with its bulk charge density. This relationship will be used in eq. (4-11) and will be discussed later.

As shown in Table 4.2, manganese which has the most considerable difference in EWF between itself and Si_3N_4 exhibits the most significant adhesive force with silicon nitride. Fig. 4.3 shows a linear relationship between the EWF and adhesive force of the metals; bear in mind that the more significant the EWF, the smaller the difference in EWF between the metal and Si_3N_4. Although the calculation was performed assuming that all materials have a natural screening length of 1 nm, the model captures the main point, i.e., the dependence of the adhesive force on the difference in work function. One may see in Fig. 4.3 that the model overestimates the adhesive force for manganese and vanadium, underestimates the adhesive force for Iron, Copper, and Silicon.

We attribute this bias to the screening length effect. The screening effect occurs when electrons –many in number - screen out other electrons from the interior of the materials coming to the interface due to the same-charge repulsion force. Electrons at the interface may also repel their neighboring electrons if the $\rho_{e\text{-int}}$ is sufficiently large since the spatial room for the electrons becomes crowded as more and more electrons move into the limited space. Based on the discussion given earlier, to correct the bias, we let d be a function of the product of relative conductivity and $\rho_{e\text{-bulk}}$. Fig. 4.4 illustrates such a relationship.
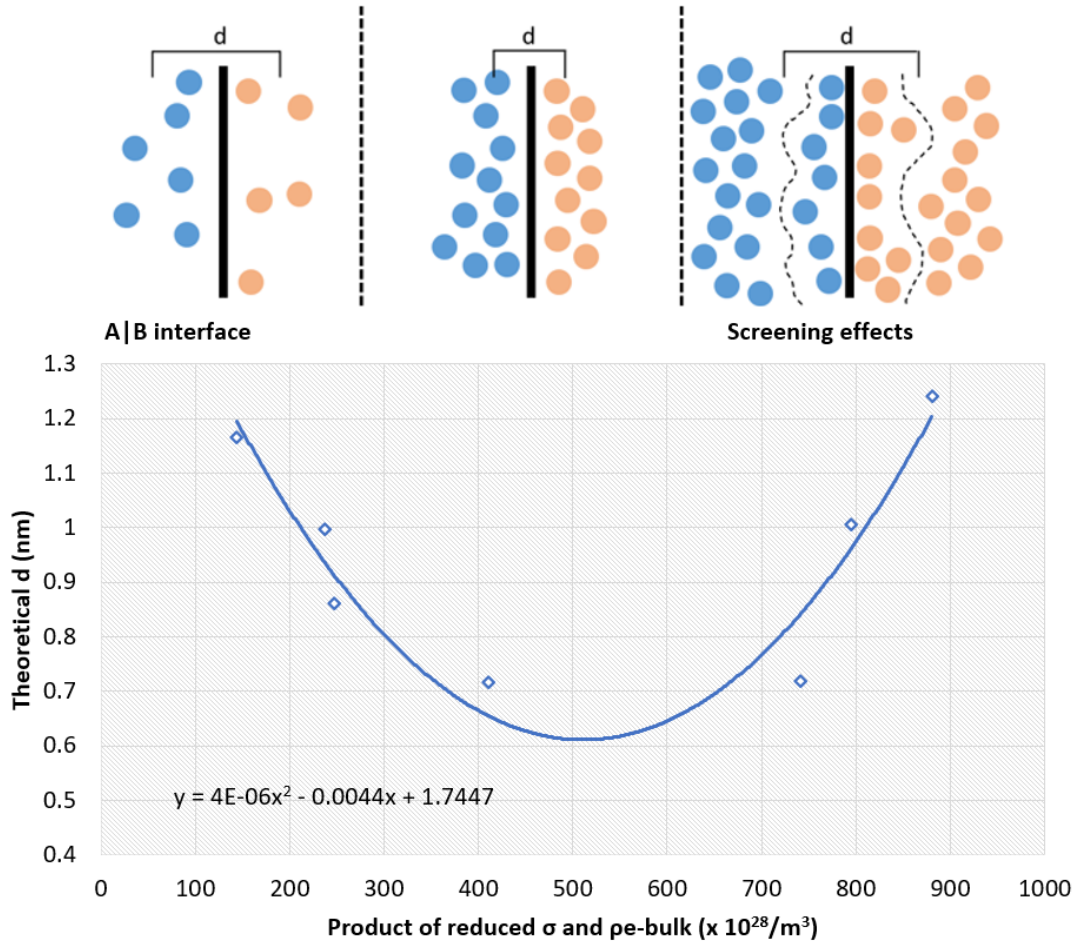
Figure 4.4. *Quadratic relation between theoretical charge separation distance and the product of relative conductivity and $\rho_{e\text{-}bulk}$; the screening effect occurs when the product of both physical properties is large, approximately over 550 x 10^{28}/m³.*

The physical interpretation for such a relationship between d and $\rho_{e-bulk}(m_A) \cdot \tilde{\sigma}(m_A)$ can be further elaborated as follows. The product of the reduced conductivity with its bulk electron density reflects both the ability of the electron to move to the interface and the number of electrons available to be catered to the interface, respectively. The width of the dipole layer would decrease with an increase in conductivity since electrons may have even higher freedom to move. However, on the other hand, increasing the electron density would increase the difficulty for electrons to be

accumulated in the vicinity of the interface due to the charge shielding effect. This may also be seen from an analytic expression of screening length in a conducting body (known as Thomas-Fermi (TF) screening) [101-102], which is given as:

$$d = \frac{1}{2e} \sqrt{\frac{k_B T}{\pi \rho_{e-int}}} \tag{4 - 12}$$

As more electrons approach the interface, they start to shield the electrons from the interior, thus enlarging the width of the dipole layer. Charges found beyond the screening length may be discarded in relevant calculations since they are being screened out by the charges at the interface and may not partake in the interfacial adhesion. Based on the above discussion, we reduce the charge separation bias on the F_{Ad} calculation and use eq. (4-13), which is a modified form of eq. (4-11), by incorporating the separation length as $\rho_{e-bulk}(m_A) \cdot \tilde{\sigma}(m_A)$:

$$
\begin{aligned}
F_{Ad} &= \frac{\varepsilon \varepsilon_0 \, A_c}{2\{f[\rho_{e-bulk}(m_A), \, \tilde{\sigma}(m_A), \, C]\}^2} \left(\frac{\varphi(m_B) - \varphi(m_A)}{e} \right)^2 \\
&\approx \frac{\varepsilon \varepsilon_0 \, A_c}{2\left[\frac{\rho N_{Av} \Sigma_{val}}{A_r}(m_A) \cdot \tilde{\sigma}(m_A), C \right]^2} \left(\frac{\varphi(m_B) - \varphi(m_A)}{e} \right)^2 \tag{4 - 13}
\end{aligned}
$$

C for Si_3N_4 is evaluated as 9.36 x $10^{-5}/m^2$, by using the sheet conductivity of Si_3N_4 [103] and its surface charge density [104]. Employing different counter-body will warrant a C of varying value, which will affect the overall fine-tuning curve of the abovementioned model—results arising from the calculation using eq. (4-13) are illustrated in Fig. 4.5, and its values are given in Table 4.3. As demonstrated, the calculated F_{Ad} is ameliorated (with the error ranging from 1.3% to 17.6 %), and better fits the measured F_{Ad} with an average error of ±7.7% and a standard deviation of 7.8% for all

the 7 metals. Thus, the fine-tuning is confirmed based on the calculation - experiment comparison and theoretical reasoning. Such a model can be extended to other material(s) of interest (illustrated by Figs. 4.6 and 4.7).
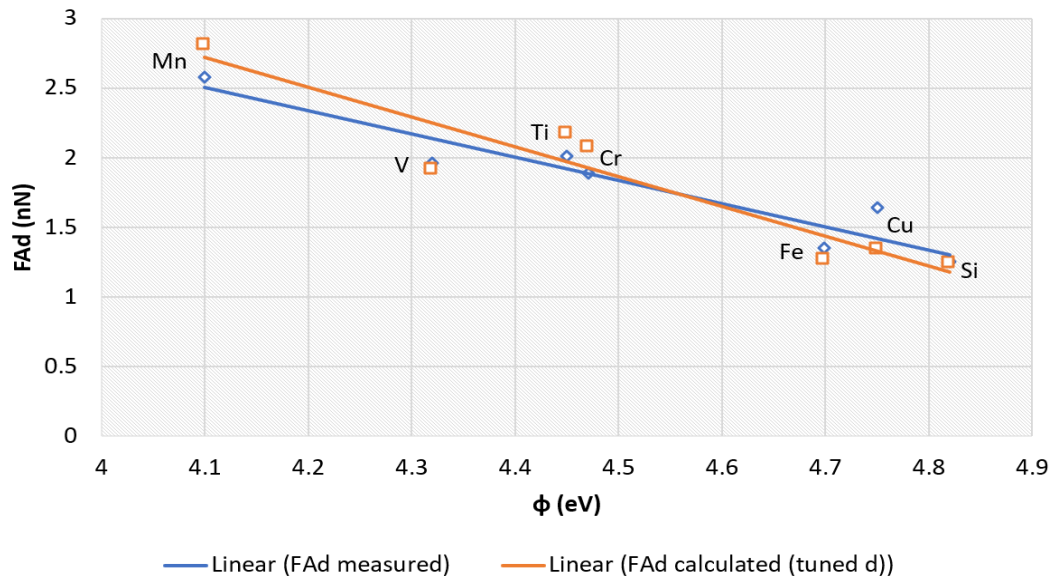
Figure 4.5. *Experiment data plotted against φ with the F_{Ad} calculated using the theoretical model with fine-tuned d using eq. (4-13).*

Table 4.3. *Adhesion force as calculated with fine-tuned d.*

Elements	F_{Ad} (measured) (nN)	F_{Ad} (calculated) with reintroduced tuned d	Error
Iron (Fe)	1.354 ± 0.18	1.260	-7.460%
Chromium (Cr)	1.888 ± 0.22	2.076	+9.055%
Manganese (Mn)	2.587 ± 0.16	2.805	+7.771%
Copper (Cu)	1.632 ± 0.11	1.345	-17.58%
Titanium (Ti)	2.006 ± 0.20	2.174	+8.375%
Vanadium (V)	1.963 ± 0.22	1.917	-2.343%
Silicon (Si)	1.251 ± 0.15	1.235	+1.295 %
		Average error	±7.697%
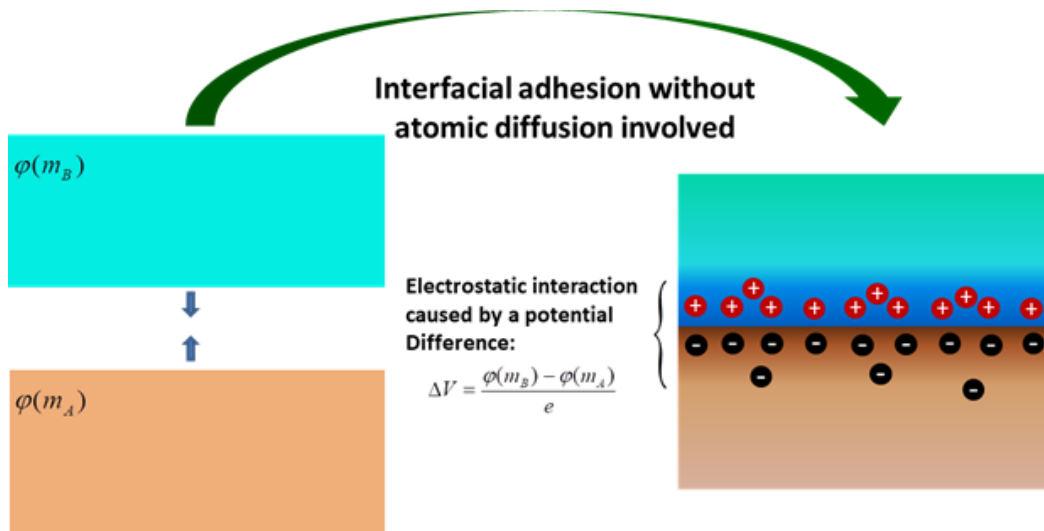
Figure 4.6. *When two different materials approach each other, the difference in their Electron Work Function is the origin for establishing interfacial adhesion or bonding. The availability and freedom of charges influence the interfacial adhesion/bonding.*
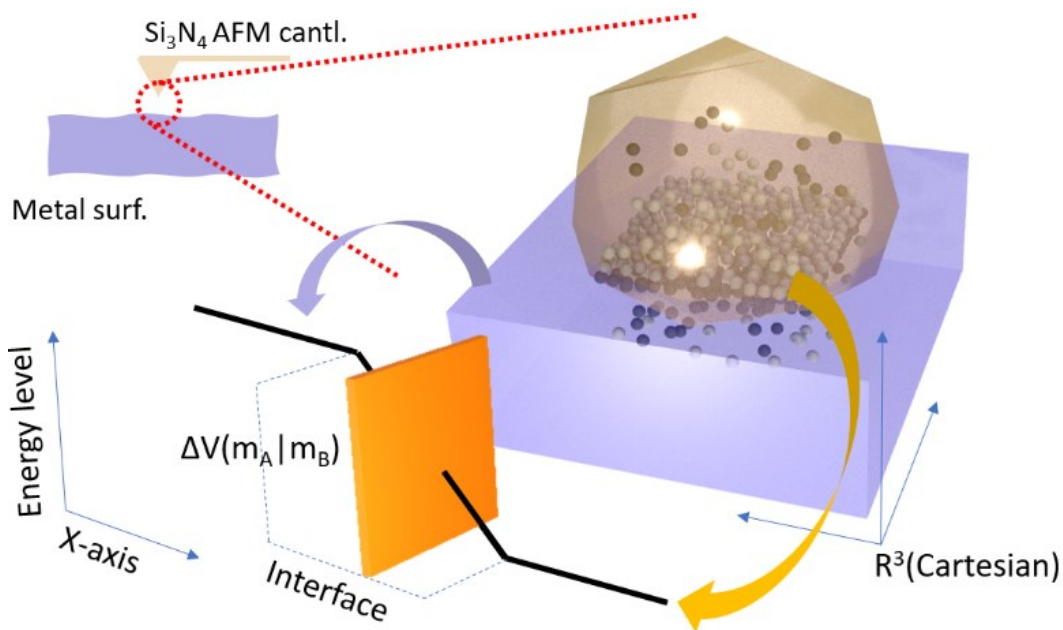
Figure 4.7. *Dipole layer forming across the interface of two materials with different EWFs.*

Chapter V:
General Conclusions

In this chapter, the results of the current works are summarized and concluded. This part states the answers to the main research questions. It will determine whether the objectives laid out as the criteria of this study's success have been met or not. It will also show new pieces of knowledge that this study has managed to contribute.

Potential future work arising from the studies conducted will also be presented. Several recommendations will be laid out to any future efforts looking to perfect the theoretical model shown in this study and for any practical usage that may arise from these studies. Furthermore, elaborations on the impact and relevance to similar studies will be presented as the remarking commentaries.

5.1. Part I: PEDOT:PSS/PEO Adhesion with Si_3N_4-Modified AFM Cantilever

5.1.1. Concluding results

The novel approach has been demonstrated to effectively enhance the interfacial bonding between two different materials in contact without atomic diffusion involved. The interfacial adherence is dependent on two main factors:

1. The difference in Electron Work Function results in a potential difference that drives charge relocation, forming a dipole layer at the interface.

2. The charge mobility or electrical conductivity facilitates the charge migration.

5.1.2. Importance and novelties

The observed enhancement has demonstrated the approach's effectiveness in interfacial bonding between Si_3N_4 and the PEDOT:PSS/PEO nanofilm. With the addition of DMSO, the nanofilm's conductivity is increased with the accompanying of lowered work function and the fact that the interfacial bonding is markedly increased. With the changes in these two factors, more electrons can move toward the interfacial zone, which facilitates the formation of a dipole layer, leading to enhanced interfacial bonding/adhesion.

It is anticipated that this new approach will find a wide range of applications in bio-medical coatings and functional devices.

5.1.3. Future works

Possible future works can be directed toward:
1. The investigation on the effect of different solvation agents toward the effect it imposes on the adhesion between PEDOT:PSS/PEO polymeric nanosheet and Si_3N_4. Different solvation products may include, i.e., sorbitol, methanol, ethanol, among many others.

2. Investigating the adhesion between PEDOT:PSS/PEO polymeric nanosheet and different metals of interest, i.e., Titanium alloy. The

69

method we propose in this study may be modified to accommodate such an investigation by directly replacing the Si_3N_4 balls on the AFM cantilever probe with the materials of interest (such as titanium or carbon nanoparticles). Such an approach may provide us with a new insight on the effect of adhesion of PEDOT:PSS/PEO with a more practical application, i.e., biomedical implants or organic solar cells.

3. Aside from the Electron Work Function (EWF) probing, we also recommend the investigation on the effect of solvation toward the changes in the polymeric nanosheet Density of States (DOS) and hopping length (ξ'). An appropriate model has been enunciated in the preceding chapter (the Electron/Charges Variable Hopping Model - VHM). By fitting the data into this model, hopefully a causation between solvation treatment and increased DOS will be established. Furthermore, this approach will provide insight into the conductivity and adhesive behavior from the quantum mechanical point of view.

5.1.4. Recommendations

Examining the observed phenomena in our study, we recommend choosing PEDOT:PSS/PEO polymeric nanosheet treated with 5% wt./wt. DMSO since it provides the highest conductivity among all other candidates demonstrates the highest interfacial adhesive profile with Silicon Nitride. We recommend that any different material design incorporating an interface between the conductive polymer and any ceramic base consider these facts.

Furthermore, during the fabrication process, we found through numerous trials-and-errors that mixing PEO with PEDOT:PSS constitutes a rigorous process of high-speed homogenizing; hence a high control of the temperature of the water bath and the homogenizer rod is a must. We

recommend a temperature of 2-4°C as the optimum range for the homogenization process. Any temperature lower than 2°C may induce the crystallization process inside the mother aliquot, while a higher temperature may start heat-induced polymer breakdown.

We recommend differentiating the spinning into three different and distinctive rotational speeds as the spin coating procedure. The first step is to start with a very low rotational speed, particularly in the range of 100-500 rpm to spread the dropped aliquot throughout the base material uniformly. The time required for this step can be modified according to the base material diameter. The second step is the high-speed rotation, where the speed is ramped up until 3,000 – 5,000 rpm for 30 seconds. The third stage is ramping down or up the speed until 30-35% of the preceding stage's rotational speed.

It is also recommended that the curing of the polymeric sheet be done inside a vacuum chamber that is well insulated against the light. This approach may prevent further oxidation processes during the process and may prevent the polymer from being broken down by light during the heat curing.

5.1.5. Remarks

This study on the adhesive interaction between Si_3N_4 and a polymeric film shows the dependence of interfacial bonding between two different types of material on the difference in EWF and the electrical conductivity. The study demonstrates a novel approach for enhancing interfacial adhesion between different kinds of material with little or without atomic diffusion in the interfacial zone. Improving the interfacial bonding can be achieved by increasing 1) the difference in EWF between the two materials in contact and 2) the electrical conductivity of the materials.

This approach is promising for improving the adherence of functional films/coatings for medical implants and organic-based solar cells

and a printable conductive ink. In principle, the more significant the difference in work function between the two materials in contact, the larger the driving force for establishing the dipole layer. However, the formation of the dipole layer cannot be achieved if electrons cannot move. Therefore, the lower the EWF, the freer the electrons. Thus, when a conductive polymer is in contact with a ceramic material that usually has a higher EWF than the conductive polymer, the lower the EWF of the polymer is, the larger the driving force will be freer is its electrons.

An enormous difference in EWF between the two materials in contact would help develop a more robust interfacial adhesive profile. However, tuning the EWF may influence other properties of materials, e.g., physical, and chemical properties, which may also be of importance to some specific applications of the materials. Thus, careful considerations are needed to obtain an appropriate balance among different properties for optimal performance.

PEDOT:PSS has found considerable usage in biomedical engineering settings. PEDOT:PSS is also an ideal material to be electro-spun for various applications such as the tissue scaffold for engineered tissue growth. The increase in interfacial adhesion as described in this study would help material selection and modification towards a widened range of applications. Moreover, this approach can also guide other endeavors to create a sturdier material for organic-based solar cells.

It should be mentioned here that significant efforts have been made to tune the energy barrier of PEDOT:PSS charge transport, e.g., the study by Kim, et.al.[88] describes the usage of polar solvent vapor annealing to tune the barrier energy in PEDOT:PSS/Bi_2Te_3 nanowires-based thermoelectric nanocomposite thin films. A study by Lee, *et al.* [89] shows that enhanced thermoelectric performance of PEDOT:PSS/PANI-CSA polymer can be achieved using multiple solution processes to fabricate the resulting compound.

Our present study demonstrates an effective way to increase the interfacial binding so that thicker PEDOT:PSS/PANI-CSA layer can be

achieved, which would help improve the effectiveness with more functions in the utilization of the material. Yeo *et al.* [90] studied the conductivity and EWF in PEDOT:PSS for an ITO-free optoelectronic system using vertical phase separation in a solvent-vapor-annealed composite film.

By tuning the conductivity and the EWF, we were able to modify the interfacial bonding based on the electrical properties alone. Such correlation between electronic properties and the interfacial mechanical interactions demonstrated in this study opens a new door for the tailoring of interfacial mechanical interaction on any feasible electronic systems, which would benefit not only the PEDOT:PSS-based optoelectronic systems but also other relevant systems that use different conductive materials as its principal base material.

5.2. Part II: Pure metals adhesive profile with Si_3N_4

5.2.1. Concluding results

The interfacial adhesive force between two materials in contact without atomic diffusion is investigated using metal-Si_3N_4 as a sample system. The following conclusions are drawn:

1. The interfacial adhesive force between two materials in contact without atomic diffusion is attributed to the formation of the dipole-dipole moment due to the electrostatic interaction. The formation of the dipole layer is by large driven by the difference in work function between the two materials. Electrons tend to move from the low-EWF material towards the one having a higher EWF.

2. The magnitude of the adhesive force is determined not only by the difference in EWF between the two materials in contact but also the charge freedom, which is reflected by the electrical conductivity, and the

charge availability which is reflected by the bulk electron density. However, if the electron density is sufficiently high, the adhesive force cannot be continuously increased due to the prominence of the charge shielding effect.

3. An analytical model is proposed to determine the interfacial adhesive force based on the dependence of F_{Ad} on the difference in EWF between the two materials in contact. The interfacial adhesive force resulting from the interfacial electrostatic interaction is influenced by the charge separation distance, which is correlated with the product of relative conductivity and electron density.

5.2.2. Importance and novelties

This study provides the new theoretical background behind the mechanism of adhesion facilitated by a dipole-dipole interaction across the interface of two different materials (i.e., pure metals with ceramics). Due to their differing EWF, the resulting electrostatic potential acts as the driving factor for the formation of the said dipole-dipole interaction.

A new model is provided in the form of an equation that correlates the interfacial adhesion force (F_{Ad}) with the contact area (A_c), medium permittivity, Boltzmann's constant (k_B), absolute ambient temperature (T), the EWF of the two materials ($\varphi(m_A)$ and $\varphi(m_B)$), the screening distance (d) and the charges density adjacent to the interface (ρ_e).

5.2.3. Future works

Future works may include the following:

1. Expanding the scope of the project beyond the already-studied seven materials in this study. This approach may further provide an ever broader and in-depth insight on the theoretical analyses. It may provide more data points to be fitted into the model, which may further corroborate our theoretical model.

2. We also seek to determine the analytical way to measure the contact area between the silicon nitride balls attached to the AFM cantilever with the material's surface. In this presentation, we argue that the contact area may be approximated as half of the sphere of that of the silicon nitride balls with its diameter already known. Possible measuring techniques that can be used to determine the contact area might include using TEM or conductive AFM (cAFM) probing.

3. Further studies may also be directed toward an analytical way to calculate or estimate the effect of metals conductivity, bulk charges density, and interfacial charges density adjacent to the surface with a separation distance analogous to that of the Thomas-Fermi (TF) screening distance. Hopefully, this will further fine-tune the model presented in this study and provide a more theoretical-based approach.

5.2.4. Recommendations

By examining our findings, the overall interfacial adhesive force can be increased with the following approaches:

1. Increase the Electron Work Function (EWF) difference across the interface corresponding to a more significant driving force for the formation of the dipole-dipole layer at the interface. This could be achieved by modifying the materials through element doping.

2. Increase the contact area (interfacial area). Our model indicates that a more significant adhesion force correlates to a wider interfacial area since it provides more interfacial dipole-dipole interaction, contributing to a higher adhesion force.

3. Increase the density and freedom of charges to facilitate the formation of the dipole-dipole layer. For instance, by increasing the conductivity of the polymeric materials or by element-doping to improve both the bulk charge density and the conductivity for any given ceramic materials.

Bibliography

1. Wang W, Xia SS, Liu GP, Gu XH, Jin WQ, Xu NP. Interfacial adhesion between polymer separation layer and ceramic support for composite membrane. *AlChE Journal*, 2019, **56**(6):1584-1592.

2. Nagamatsu KA, Avasthi S, Jhaveri J, Sturm JC. A 12% Efficient Silicon/PEDOT:PSS Heterojunction Solar Cell Fabricated at < 100 °C. *IEEE Journal of Photovoltaics*, 2013, **4**(1):260-264.

3. Wang L., Duan F. Nanoscale wear mechanisms of few-layer graphene sheets induced by interfacial adhesion. *Tribology International*, 2018, **123**:266-272.

4. Milanese E, Brink T, Aghababaei R, Molinari JF. Role of interfacial adhesion on minimum wear particle size and roughness evolution. *Phys. Rev. E.*, 2020, **102**(4).

5. Rokni H, Lu W. Direct measurements of interfacial adhesion in 2D materials and van der Waals heterostructures in ambient air. *Nature Communications*, 2020, **11**:5607.

6. Fabio LL, Bueno CC, Da Róz AL, Ziemath EC, Oliveira-Jr. ON. Theoretical Models for Surface Forces and Adhesion and Their Measurement Using Atomic Force Microscopy. *Int. J. Mol. Sci.*, 2012, **13**(10): 12773-12856.

7. Purcell E. Electricity and Magnetism. *Cambridge University Press*, London, 2011.

8. Xu S., Nogogaki T, Tachi K, Sato S, Miyata I, Yamanaka J, Yonese M. Two dimensional auto-organized nanostructure formation of acid polysaccharides on bovine serum albumin monolayer and its surface tension. *Studies in Surface Science and Catalysis*, 2001, **132**:889-892.

9. Parker GW. Derivation of the electric dipole–dipole interaction as an electric hyperfine interaction. *American J. of Physics*, 1986, **54**: 75.

10. Israelachvili JN. Intermolecular and Surface Forces (2nd ed.) *Academic Press*, Santa Barbara, CA, 1995.

11. Zhu DM, Eastman T. Adhesion Forces between Surface-Modified AFM Tips and a Mica Surface. *Langmuir*, 1996, **12**(11): 2859-2862.

12. Hua G, Li DY. Generic relation between the electron work function and Young's modulus of metals. *Appl. Phys. Lett.*, 2011, **99**: 041907.

13. Setiawan RC, Li DY. Tuning the Conductivity and Electron Work Function of a Spin-Coated PEDOT:PSS/PEO Nanofilm for Enhanced Interfacial Adhesion. *Langmuir*, 2021, **37**: 4924-4932.

14. Moy TV, Florin EL, Gaub HE. Adhesive forces between ligand and receptor measured by AFM. *Colloids and Surfaces A*, 2001, **93**: 343-348.

15. Götzinger M, Peukert W. Particle Adhesion Force Distributions on Rough Surfaces. *Langmuir*, 2004, **20**(13): 5298-5303.

16. Senden TJ, Drummond CJ. Surface chemistry and tip-sample interactions in atomic force microscopy. *Colloids and Surfaces A*, 1995, **94**(1): 29-51.

17. Folch A, Wrighton MS, Schmidt MA. Microfabrication of oxidation-sharpened silicon tips on silicon nitride cantilevers for atomic force microscopy. *IEEE*, 1997, 6(4): 303-306.

18. Li Y, Li DY. Experimental studies on relationships between the electron work function, adhesion, and friction for 3d transition metals. *J. Appl. Physics*, 2004, **95**: 7961.

19. Grow RJ, Minne SC, Manalis SR, Quate CF. Silicon nitride cantilevers with oxidation-sharpened silicon tips for atomic force microscopy. *IEEE*, 2002, **11**(4): 317-321.

20. Conache G, Gray SM, Ribayrol A, Fröberg LE, Samuelson L, Pettersson H, Montelius L. Friction Measurements of InAs Nanowires on Silicon Nitride by AFM Manipulation. *Nano Micro Small*, 2009, **5**(2): 203-207.

21. Bikerman JJ. XXXIX. Structure and capacity of electrical double layer. *The London, Edinburgh, and Dublin Philosophical Magazine and Journal of Science*, 1942, **33**(220): 384-397.

22. Kasap S, Koughia C, Ruda HE. Electrical Conduction in Metals and Semiconductors. *Springer Handbook of Electronic and Photonic Materials*, 2017.

23. van der Werf KO, Putman CAJ, de Grooth BG, Greve J. Adhesion force imaging in air and liquid by adhesion mode atomic force microscopy. *Appl. Phys. Lett.*, 1994, **65**: 1995.

24. Persson BNJ, The dependency of adhesion and friction on electrostatic attraction. *The Journal of Chemical Physics*, 2018, **148**: 144701.

25. Oláh A, Vancso GJ. Characterization of adhesion at solid surfaces: Development of an adhesion-testing device. *European Polymer Journal*, 2005, **41**(12): 2803-2823.

26. Wei W, Xia SS, Liu GP, Jin WQ, Xu NP. Interfacial adhesion between polymer separation layer and ceramic support for composite membrane. *Materials, Interfaces, and Electrochemical Phenomena*, 2009, **56**(6): 1584-1592.

27. Israelachvili JN, McGuiggan PM. Adhesion and short-range forces between surfaces. Part I: New apparatus for surface force measurements. *Journal of Materials Research*, 2011, **5**(10).

28. IUPAC. Compendium of Chemical Terminology, 2nd ed. (the "Gold Book"). Compiled by A. D. McNaught and A. Wilkinson. *Blackwell Scientific Publications*, Oxford, 1997. Online version (2019-) created by Chalk SJ. ISBN 0-9678550-9-8. https://doi.org/10.1351/goldbook.

29. Israelachvili JN. Intermolecular and Surface Forces. *Academic Press, New York*, 1985, Chapter 15.

30. Schrader ME. Young-Dupre Revisited. *Langmuir*, 1995, **11**: 3585-3589.

31. Leng YS, Jiang SY. Dynamic Simulations of Adhesion and Friction in Chemical Force Microscopy. *J. Am. Chem. Soc.*, 2002, **124**(39): 11764–11770.

32. Kim WS, Yun IH, Lee JJ, Jung HT. Evaluation of mechanical interlock effect on adhesion strength of polymer–metal interfaces using micro-patterned surface topography. *International Journal of Adhesion and Adhesives*, 2010, **30**(6): 408-417.

33. Lee LH. Adhesive Bonding. *Plenum Press*, New York, 1991, Chapter 19.

34. Wang J, Gao H. Clustering instability in adhesive contact between elastic solids via diffusive molecular bonds. *Journal of the Mechanics and Physics of Solids*. 2008, **56**(1): 251-266.

35. Yang Y, Erb RM, Wiley BJ, Zauscher S, Yellen BB. Imaginary Magnetic Tweezers for Massively Parallel Surface Adhesion Spectroscopy. *Nano Lett.*, 2011, **11**(4): 1681–1684.

36. Fällman E, Schedin S, Jass J, Andersson M, Uhlin BE, Axner O. Optical tweezers based force measurement system for quantitating binding interactions: system design and application for the study of bacterial adhesion. *Biosens. Bioelectron.*, 2004, **19**(11): 1429-1437.

37. Shao JY, Xu G, Guo P. Quantifying Cell-Adhesion Strength with Micropipette Manipulation: Principle and Application. *Frontiers in Bioscience*, 2004, **9**: 2183-2191.

38. Kamsma D, Bochet P, Oswald F, Alblas N, Goyard S, Wuite GJL, Peterman EJG, Rose T. Single-Cell Acoustic Force Spectroscopy: Resolving Kinetics and Strength of T Cell Adhesion to Fibronectin. *Cell Reports*, 2018, **24**(11): 3008-3016.

39. Matthews BD, Overby DR, Alenghat FJ, Karavitis J, Numaguchi Y, Allen PG, Ingber DE. Mechanical properties of individual focal adhesions probed with a magnetic microneedle. *Biochemical and Biophysical Research Communications*, 2004, **313**(3): 758-764.

40. Dufrêne YF. Atomic Force Microscopy, a Powerful Tool in Microbiology. *J. Bacteriol*, 2002, 184(19): 5205-5213.

41. Tang Z. Studies of Inverted Organic Solar Cells Fabricated by Doctor Blading Technique. Materials Science, Independent thesis, 2010.

42. Bruker AFM Probes. Silicon Nitride Probes. https://www.brukerafmprobes.com/c-111-silicon-nitride-probes.aspx, retrieved 2021-08-04, accessed in August 2021.

43. Olympus. Micro cantilever for DC (contact) mode AFM and LFM. https://www2.mpip-mainz.mpg.de/~rietzler/Cantilever/OMCL-TR800PSA-1.html, retrieved 2021-08-04. Accessed in August 2021.

44. Jiang Y, Turner KT. Measurement of the strength and range of adhesion using atomic force microscopy. *Extreme Mechanics Letters*, 2016, **9**(1): 119-126.

45. Kittel C. Introduction to Solid State Physics (8th ed.) *John Wiley and Sons*. 2015, ISBN: 978-1-119-45416-8.

46. Torre C. PHYS 3700: Introduction to Quantum Statistical Thermodynamics. Utah State University, 2015. Retrieved August 2021.

47. Ashcroft NW, Mermin ND. Solid State Physics. *Holt, Rinehart and Winston*, 1976, ISBN: 978-0-03-083993-1.

48. Luo Y, Tang Y, Chung TF, Tai CL, Chen CY, Yang JR, Li DY. Electron work function: an indicative parameter towards a novel material design methodology. *Scientific Reports*, 2021, **11**: 11565.

49. Lu H, Li DY. Correlation between the electron work function of metals and their bulk moduli, thermal expansion and heat capacity via the Lennard–Jones potential. *Physica Status Solidi (b)*, 2014, **251**(4).

50. Al-Ahmadi NA. Metal oxide semiconductor-based Schottky diodes: a review of recent advances. *Materials Research Express*, 2020, 7(3): 032001.

51. Semenikhin OA, Jiang L, Iyoda T, Hashimoto K, Fujishima A. Atomic Force Microscopy and Kelvin Probe Force Microscopy Evidence of Local Structural Inhomogeneity and Nonuniform Dopant Distribution in Conducting Polybithiophene. *J. Phys. Chem.*, 1996, **100**(48): 18603–18606.

52. Nonnenmacher M, O'Boyle MP, Wickramasinghe HK. Kelvin probe force microscopy. *Appl. Phys. Lett.*, 1991, **58**: 2921.

53. Larisa-Emilia C, Sherri J, Saman S, Michael T. Work-function measurement by high-resolution scanning Kelvin nanoprobe. *Measurement Science and Technology*, 2007, **18**(3): 567–578.

54. Fernández Garrillo P. A., Grévin B., Chevalier, N., Borowik, Ł. Calibrated work function mapping by Kelvin probe force microscopy. *Review of Scientific Instruments*. 2018. **89**(4): 043702.

55. Zisman, W. A., A NEW METHOD OF MEASURING CONTACT POTENTIAL DIFFERENCES IN METALS. *Review of Scientific Instruments*, 1932, **3**(7): 367–370.

56. Li J, Liu JC, Gao CJ. On the mechanism of conductivity enhancement in PEDOT/PSS film doped with multi-walled carbon nanotubes. *Journal of Polymer Research*, 2010, **17**: 713-718.

57. Lee I, Kim GW, Yan M, Kim T-S. Simultaneously Enhancing the Cohesion and Electrical Conductivity of PEDOT:PSS Conductive Polymer Films using DMSO Additives. *ACS Appl. Mater. Interfaces*, 2016, **8**(1): 302-310.

58. Hokazono M, Anno H, Toshima N. Thermoelectric Properties and Thermal Stability of PEDOT:PSS Films on a Polyimide Substrate and Application in Flexible Energy Conversion Devices. *Journal of Electronic Materials*, 2014, **43**: 2196-2201.

59. Zhang X, Li C, Luo Y. Aligned/Unaligned Conducting Polymer Cryogels with Three-Dimensional Macroporous Architectures from Ice-Segregation-Induced Self-Assembly of PEDOT-PSS. *ACS Publicatin Langmuir*, 2011, **27**(5): 1915-1923.

60. Vosgueritchian M, Lipomi DJ, Bao Z. Highly Conductive and Transparent PEDOT:PSS Films with a Fluorosurfactant for Stretchable and Flexible Transparent Electrodes. *Advanced Functional Materials*, 2012, **22**(2): 421-428.

61. Yildrim E, *et.al*. A theoretical mechanistic study on electrical conductivity enhancement of DMSO treated PEDOT:PSS. *J. Mater. Chem. C.*, 2018, **6**(19): 5122-5131.

62. Yazdimamaghani M, Razavi M, Mozafari M, Vashaee D, Kotturi H, Tayebi L. Biomineralization and biocompatibility studies of bone conductive scaffolds containing poly(3,4-ethylenedioxythiophene):poly(4-styrene sulfonate) (PEDOT:PSS). *J. Mater. Sci: Materials in Medicine*, 2015, **26:** 274.

63. Kumar Saurabh, Umar Mohammad, Saifi Anas, Kumar Suveen, Augustine Shine, Srivastava Saurabh, Malhotra BD. Electrochemical paper based cancer biosensor using iron oxide nanoparticles decorated PEDOT:PSS. *Analytica Chimica Acta*, 2019, **1056**: 135-145.

64. Hu Y, Cheng W Highly Conductive PEDOT/PSS Thin Films for Potential Organic Transparent Electrodes of Touchscreens. *Recent Patents on Materials Science*, 2013, **6**(1): 68-74.

65. Heo DN, Lee S-J, Timsina R, Qiu XY, Castro NJ, Zhang LG. Development of 3D printable conductive hydrogel with crystallized PEDOT:PSS for neural tissue engineering *Mater. Sci. and Eng.: C.*, 2019, **99**: 582-590.

66. Guan G, Yang Z, Qiu L, Sun X, Zhang Z, Ren J, Peng H. Oriented PEDOT:PSS on aligned carbon nanotubes for efficient dye-sensitized solar cells. *J. Mater. Chem. A.*, 2013, **1**: 13268-13273.

67. Pires F, Ferreira Q, Rodrigues CAV, Morgado J, Ferreira FC. Neural stem cell differentiation by electrical stimulation using a cross-linked PEDOT substrate: Expanding the use of biocompatible conjugated conductive polymers for neural tissue engineering. *Biochimica et Biophysica Acta (BBA) – General Subjects*, 2015, **1850**(6): 1158-1168.

68. Kim SM, Kim N, Kim YS, Baik MS, Yoo M, Kim DY, Lee WJ, Kang DH, Kim S, Lee KH, Yoon MH. High-performance, polymer-based direct cellular interfaces for electrical stimulation and recording. *NPG Asia Materials*, 2018, **10**: 255-265.

69. Hong W, Xu Y, Lu G, Li C, Shi G. Transparent graphene/PEDOT–PSS composite films as counter electrodes of dye-sensitized solar cells. *Electrochemistry Communications*, 2008, **10**(10): 1555-1558.

70. Zhang Y, Cui W, Zhu Y, Zu F, Liao L, Lee ST, Sun B. High efficiency hybrid PEDOT:PSS/nanostructured silicon Schottky junction solar cells by doping-free rear contact. *Energy & Environmental Sci.*, 2015, **8**: 297-302.

71. Li, DY, Guo L, Li L, Lu H, Electron work function – a probe for interfacial diagnosis, *Scientific Report-Nature*, 2017, DOI: 10.1038/s41598-017-08841-x.

72. Tseng YT, Lin YC, Shih CC, Hsieh HC, Lee WY, Chiu YC, Chen WC. Morphology and properties of PEDOT:PSS/soft polymer blends through hydrogen bonding interaction and their pressure sensor application. *J. Mater. Chem. C.*, 2020, **8**: 6013-6024.

73. Kim N, Kee S, Lee SH, Lee BH, Kahng YH, Jo YR, Kim BJ, Lee K. Highly Conductive PEDOT:PSS Nanofibrils Induced by Solution-Processed Crystallization. 2013. *Advanced Materials*, 2014, **26**(14): 2268-2272.

74. Liu Q, Ono M, Tang Z, Ishikawa R, Ueno K, Shirai H. Highly efficient crystalline silicon/Zonyl fluorosurfactant-treated organic heterojunction solar cells. *Appl. Phys. Lett.*, 2012, **100**: 183901.

75. Xia Y, Ouyang J. PEDOT:PSS films with significantly enhanced conductivities induced by preferential solvation with cosolvents and their application in polymer photovoltaic cells. *J. Mater. Chem.*, 2011, **21**: 4927-4936.

76. Cui XT, Zhou DD. Poly (3, 4-ethylenedioxythiophene) for chronic neural stimulation. *IEEE Trans. Neural Syst. Rehabil. Eng.*, 2007, **15**: 502-508.

77. Liu N, Fang GJ, Wan JW, Zhou H, Long H, Zhao XZ. *J. Mater. Chem.*, 2011, **21**: 18962-18966.

78. Sousa PM, Gutiérrez M, Mendoza E, Llobera A, Chu V, Conde JP. Integration of Carbon Nanotubes into Electrostatically Actuated all-Polymer PEDOT: PSS/PMMA MEMS. *Procedia Engineering*, 2011, **25**: 1665-1668.

79. Cárdenas-Martíneza J, España-Sánchez BL, Esparzac R, Ávila-Niño JA. Flexible and transparent supercapacitors using electrospun PEDOT:PSS electrodes. *Synthetic Metals*, 2020, **267**: 116436.

80. Webb K, Hlady V, Tresco PA. Relative importance of surface wettability and charged functional groups on NIH 3T3 fibroblast attachment, spreading, and cytoskeletal organization. *J. Biomed Mater Res.*, 1998, **41**(3): 422–430.

81. Mu Y, Zhang Y, Zhang H, Li Z. Characterization of PEDOT:PSS as a biocompatible conductive material. *10th IEEE International Conference on Nano/Micro Engineered and Molecular Systems, Xi'an*, 2015, pp. 149-151, DOI: 10.1109/NEMS.2015.7147397.

82. Nardes AM, Janssen RAJ, Kemerink M. A Morphological Model for the Solvent-Enhanced Conductivity of PEDOT:PSS Thin Films. *Advanced Functional Materials*, 2008, **18**(6): 865-871.

83. Guo LQ, Hua GM, Yang BJ, Lu Hao, Qiao LJ, Yan XG, Li DY. Electron work functions of ferrite and austenite phases in a duplex stainless steel and their adhesive forces with AFM silicon probe. *Scientific Reports*, 2016, **6**: 20660.

84. Hölzl J., Schulte F. K. Work function of metals. *Solid Surface Physics*, 2006, **85**: 1-150.

85. Bauza M, Li F, Vygranenko Y, Ahnood A. Photo-Induced Instability of Nanocrystalline Silicon TFTs. *Display Technology Letters*, 2011, **6**(12): 589-591.
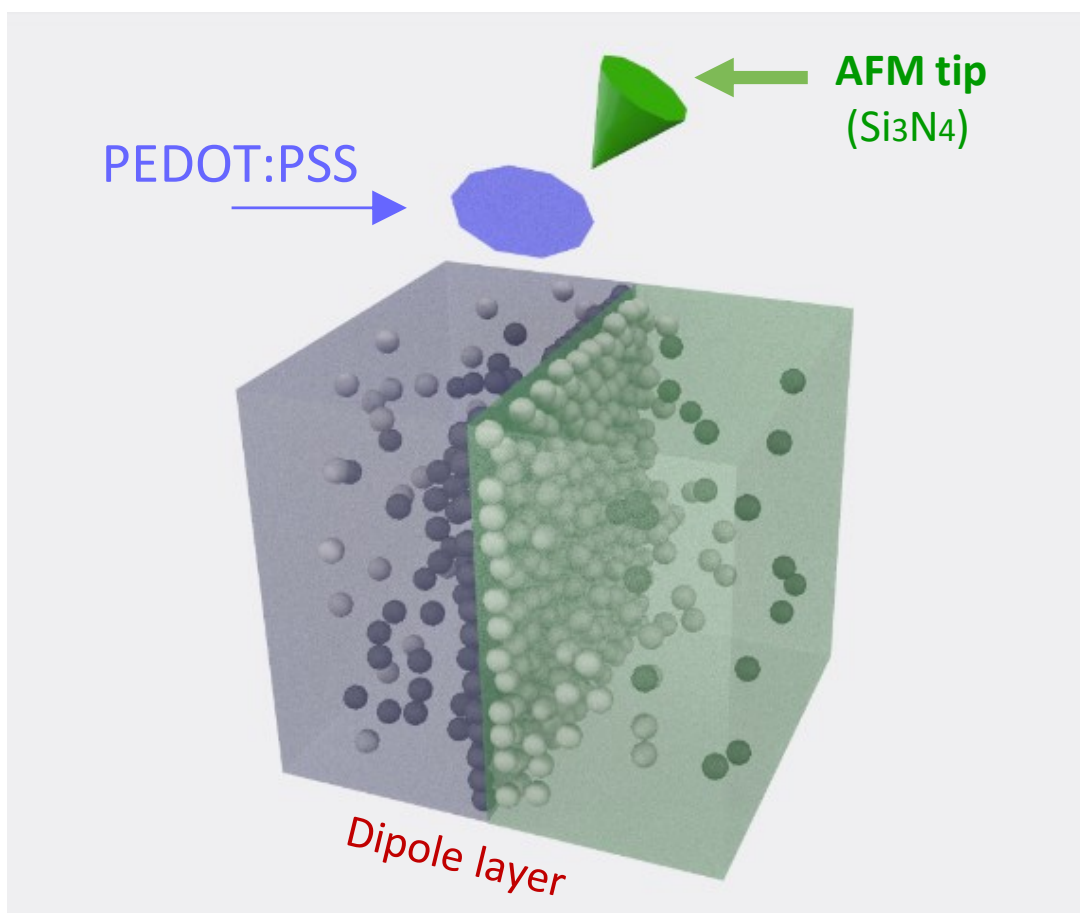
86. Cruz-cruz I, Reyes-Reyes M, Aguilar-Frutis MA, Rodriguez AG, López-Sandovald R. Study of the effect of DMSO concentration on the thickness of the PSS insulating barrier in PEDOT:PSS thin films. *Synthetic Metals*, 2010, **160**(13-14): 1501-1506.

87. Mahato S, Puigdollers J, Voz Cristobal, Mukhopadhyay M, Mukherjee M, Hazra S. Near 5% DMSO is the best: A structural investigation of PEDOT: PSS thin films with strong emphasis on surface and interface for hybrid solar cell. *Applied Surface Science*, 2020, **499**: 143967.

88. Kim WS, Anoop G, Jeong IS, Lee HJ, Kim HB, Kim SH, Goo GW, Lee H, Lee HJ, Kim C, Lee JH, Mun BS, Park JW, Lee E, Jo JY. Feasible tuning of barrier energy in PEDOT:PSS/Bi2Te3 nanowires-based thermoelectric nanocomposite thin films through polar solvent vapor annealing. *Nano Energy*, 2020, **67**: 104207.

89. Lee HJ, Anoop G, Lee HJ, Kim C, Park JW, Choi J, Kim H, Kim YJ, Lee E, Lee SG, Kim YM, Lee JH, Jo JY. Enhanced thermoelectric performance of PEDOT:PSS/PANI–CSA polymer multilayer structures. *Energy Environ. Sci.*, 2016, **9**: 2806-2811.

90. Yeo JS, Yun JM, Kim DY, Park S, Kim SS, Yoon MH, Kim TW, Na SI. Significant Vertical Phase Separation in Solvent-Vapor-Annealed Poly(3,4-ethylenedioxythiophene):Poly(styrene sulfonate) Composite Films Leading to Better Conductivity and Work Function for High-Performance Indium Tin Oxide-Free Optoelectronics. *ACS Appl. Mater. Interfaces*, 2012, **4**(5): 2551–2560.

91. Michael B. Heaney. Electrical Conductivity and Resistivity 2nd edition. Adapted from Measurement, Instrumentation, and Sensors Handbook, edited by Webster JG and Eren H. *CRC Press*, 2014.

92. Kittel C., Introduction to Solid State Physics, 7th ed. *John Wiley & Sons*, New York, 1996.

93. Meng Y. Electrostatic Field Effects on Adhesion. In: Q. J. Wang, Y.W. Chung, (eds) Encyclopedia of Tribology, *Springer*, Boston, MA, 2013. DOI: https://doi.org/10.1007/978-0-387-92897-5_461.

94. Nikitas P. Dipole interactions in models of the dense part of the electrical double layer. *Canadian Journal of Chemistry*, 1986, **64**(7).

95. Stojek Z. The Electrical Double Layer and Its Structure. Adapted from Scholz F. (eds) *Electroanalytical Methods*, Springer, Berlin, Heidelberg. 2005. DOI: https://doi.org/10.1007/978-3-662-04757-6_1.

96. Kasap S, Koughia C, Ruda H.E. Electrical Conduction in Metals and Semiconductors. *Springer Handbook of Electronic and Photonic Materials*, Springer, 2017.

97. Kahn A. Fermi level, work function and vacuum level. *Mater. Horiz.*, 2016, **3**: 7-10.

98. Young HD, Freedman RA. University Physics with Modern Physics, 14th Edition. *Pearson*, New York, 2016, pp. 722-750.

99. Persson BNJ. The dependency of adhesion and friction on electrostatic attraction. *The Journal of Chemical Physics*, 2018, **148**: 144701.

100. Kweon HJ, Yiacoumi S, Tsouris C. The role of electrostatic charge in the adhesion of spherical particles onto planar surfaces in atmospheric systems. *Colloids and Surfaces A: Physicochemical and Engineering Aspects*, 2015, **481**: 583-590.

101. Ashcroft NW, Mermin ND. Solid State Physics. *Thomson Learning*, Toronto. 1976.

102. Grant IS, Phillips WR. Electromagnetism. Manchester Physics (2nd ed.). *John Wiley & Sons*, 2008.

103. Alam MT, Manoharan MP, Haque MA, Muratore C, Voevodin A. Influence of strain on thermal conductivity of silicon nitride thin films. *J. Micromech. Microeng.*, 2012, **22**: 045001.

104. V. Sharma. Study of Charges Present in Silicon Nitride Thin Films and Their Effect on Silicon Solar Cell Efficiencies. PhD thesis, *Arizona State University, Tempe AZ, USA*, 2013.

105. He H, Ouyang J. Enhancements in the Mechanical Stretchability and Thermoelectric Properties of PEDOT:PSS for Flexible Electronics Applications. *Acc. Mater. Res.*, 2020, **1**(2): 146-157

Appendices

Graphical abstract I:

Graphical abstract II: